

UNIVERSITY OF WARMIA AND MAZURY IN OLSZTYN

Technical Sciences

23(3) 2020

Editorial Board

Ceslovas Aksamitauskas (Vilnius Gediminas Technical University, Lithuania), Olivier Bock (Institut National de L'Information Géographique et Forestière, France), Stefan Cenkowski (University of Manitoba, Canada), Adam Chrzanowski (University of New Brunswick, Canada), Davide Ciucci (University of Milan-Bicocca, Italy), Sakamon Devahastin (King Mongkut's University of Technology Thonburi in Bangkok, Thailand), German Efremov (Moscow Open State University, Russia), Mariusz Figurski (Military University of Technology, Poland), Maorong Ge (Helmholtz-Zentrum Potsdam Deutsches GeoForschungsZentrum, Germany), Dorota Grejner-Brzezinska (The Ohio State University, USA), Janusz Laskowski (University of Life Sciences in Lublin, Poland), Arnold Norkus (Vilnius Gediminas Technical University, Lithuania), Stanisław Pabis (Warsaw University of Life Sciences-SGGW, Poland), Lech Tadeusz Polkowski (Polish-Japanese Institute of Information Technology, Poland), Arris Tijsseling (Technische Universiteit Eindhoven, Netherlands), Vladimir Tilipalov (Kaliningrad State Technical University, Russia), Alojzy Wasilewski (Koszalin University of Technology, Poland)

Editorial Committee

Marek Markowski (Editor-in-Chief), Piotr Artiemjew, Kamil Kowalczyk, Wojciech Sobieski, Piotr Srokosz, Magdalena Zielińska (Assistant Editor), Marcin Zieliński

Features Editors

Piotr Artiemjew (Information Technology), Marcin Dębowski (Environmental Engineering), Zdzisław Kaliniewicz (Biosystems Engineering), Grzegorz Królczyk (Materials Engineering), Marek Mróz (Geodesy and Cartography), Ryszard Myhan (Safety Engineering), Wojciech Sobieski (Mechanical Engineering), Piotr Srokosz (Civil Engineering), Jędrzej Trajer (Production Engineering)

Statistical Editor

Paweł Drozda

Executive Editor

Mariola Jezierska

The Technical Sciences is indexed and abstracted in BazTech (<http://baztech.icm.edu.pl>) and in IC Journal Master List (<http://journals.indexcopernicus.com>)

The Journal is available in electronic form on the web sites
<http://www.uwm.edu.pl/techsci> (subpage Issues)
<http://wydawnictwo.uwm.edu.pl> (subpage Czytelnia)

The electronic edition is the primary version of the Journal

PL ISSN 1505-4675

e-ISSN 2083-4527

© Copyright by Wydawnictwo UWM • Olsztyn 2020

Address

ul. Jana Heweliusza 14
10-718 Olsztyn-Kortowo, Poland
tel.: +48 89 523 36 61
fax: +48 89 523 34 38
e-mail: wydawca@uwm.edu.pl

Ark. wyd. 6,20, ark. druk. 5,25, nakład 75 egz.
Druk – Zakład Poligraficzny UWM, zam. 17

Contents

Z. SYROKA – <i>A controller for brushless direct current electric motors. Part 2: Software</i>	209
T. CHROSTEK – <i>Structural analysis of Fe-Al coatings applied by gas detonation spraying</i>	221
P. GORZELANCZYK – <i>Influence of selected aspects of the technical condition of means of transport operating in Wielkopolska in Poland on road safety</i>	233
W. REJMER – <i>Influence of plastic deformation on the electrochemical properties of X5CrNi18-10 steel</i>	253
K. ROJCEWICZ, Z. OKSIUTA – <i>Viability analysis of pine sawdust drying in a fountain dryer</i>	263



Quarterly peer-reviewed scientific journal

ISSN 1505-4675
e-ISSN 2083-4527

TECHNICAL SCIENCES

Homepage: www.uwm.edu.pl/techsci/



DOI: <https://doi.org/10.31648/ts.5696>

A CONTROLLER FOR BRUSHLESS DIRECT CURRENT ELECTRIC MOTORS PART 2: SOFTWARE

Zenon Syroka

ORCID: 0000-0003-3318-8495
Technical Science Department
University of Warmia and Mazury

Received 24 July 2020, accepted 1 December 2020, available online 3 December 2020.

Key words: digital control, motor controller electric and hybrid vehicles, brushless motors, microcontroller.

Abstract

A universal controller for brushless direct current (BLDC) motors was designed in the presented article. The system is controlled from the user console where operating parameters are set by the user. Signals are transmitted by cables to microcontrollers which control and monitor electric motors. Microprocessors communicate via a data bus. The controller contains the user console module and the motor control module. The user console module generates commands, and motors are controlled and monitored by the control module. Motor control modules operate independently, and each brushless motor has a dedicated control module. Brushless motors can be controlled in bipolar or unipolar mode. The control method is selected by the operator. The user console and motor controllers communicate via the I²C bus.

Correspondence: Zenon Syroka, Katedra Elektrotechniki, Energetyki, Elektroniki i Automatyki, Wydział Nauk Technicznych, Uniwersytet Warmińsko-Mazurski, ul. Oczapowskiego 11, 10-719 Olsztyn, e-mail: zenon.syroka@uwm.edu.pl, syrokaz@onet.eu

Introduction

The article consists of two parts. The first part describes the electronic and electrical design of the motor controller, and the second part presents the applied software. The described controller for brushless motors has been designed and patented by Z. SYROKA and K. KRAJEWSKI (patent No. P431380, filing date: 4 October 2019).

Industrial machines, vehicles, power tools and household appliances have motor drive elements that power mechanical components. The popularity of electric cars has been increasing in the 21st century. Batteries and motors are the key components of electric vehicles. Batteries are positioned at the bottom of the chassis to lower the vehicle's center of gravity. The motor is located in the front or at the back of the vehicle (Tesla Model S). The motors in electric cars are powered by direct (DC) or alternating current (AC). Brushless motors are one type of DC motors. Rapid advances in electrical and power engineering have introduced novel components to brushless motors, including thyristors, diodes and MOSFET transistors. Electronic subassemblies can turn power supply on and off hundreds or even thousands of times within one second. In electric bicycles, a brushless motor is placed inside the wheel hub. Power is transferred to the wheel, which reduces the physical effort associated with pedaling by 50%.

This article discusses a controller for brushless DC motors that are mounted inside the wheels of land vehicles. The motor is controlled by the user via the user console. The user can change motor speed, driving direction and deploy the electric braking system. The controller controls the steering system, the drivetrain and the braking system. Brushless DC motors can be controlled in unipolar or bipolar mode.

Microcontroller software

The controller contains three microcontrollers. Each microcontroller requires dedicated software for performing its functions. The described controller features Atmega328 microcontrollers which were programmed in the Arduino environment. The Arduino tool resembles a simple text editor, and it is divided into three main sections: toolbar, message area, and code editor. The toolbar at the top features command buttons. The code editor is where the sketches (programs) are written. The message area displays information about the status of the current sketch and possible errors.

The programs that control brushless motors have similar codes. The code for the master microcontroller is related to the user panel, and it sends commands to the microcontrollers that drive brushless motors.

Code for the master microcontroller

The master microcontroller receives and processes data from the user panel and sends commands to slave microcontrollers that drive brushless motors. The master microcontroller controls motor speed and enables the vehicle to move in different directions. The user operates push-buttons and a potentiometer on the user panel to send information about driving speed and direction to the master microcontroller. The data received by the master microcontroller is processed by algorithms and transmitted by the I²C bus to slave microcontrollers.

Microcontroller pins are identified, libraries are included and variables are added in the first step of the program (Fig. 1).

```
3 #define przod 4
4 #define tyl 5
5 #define prawo 6
6 #define lewo 7
7 #define hamulec 8
8 #define potencjometr A0
9 #include <Wire.h>
10 int predkoscAktualna, predkoscPoprzednia=0;
```

Fig. 1. Code for the master microcontroller – definitions

Command *#define* gives a name to a constant value. For example, value 4 is preceded by the name *right* because the SW1 button is connected to the pin corresponding to this value. Command *#include <Wire.h>* includes an external library in the code. The Wire library enables devices to communicate via the I²C bus. Command *int currentSpeed previousSpeed* adds two values that store information about motor speed. The setup function is described in the next step of the program (Fig. 2).

```
46 void setup() {
47   pinMode(przod, INPUT_PULLUP);
48   pinMode(tyl, INPUT_PULLUP);
49   pinMode(prawo, INPUT_PULLUP);
50   pinMode(lewo, INPUT_PULLUP);
51   pinMode(hamulec, INPUT_PULLUP);
52   Wire.begin();
53   WyborSterowania();
54 }
```

Fig. 2. Code for the master microcontroller – setup function

The *void setup* function is called when the microcontroller is powered up. The function code with the instructions to be executed is placed inside braces. Command *pinMode* (*forward*, *INPUT_PULLUP*) informs the microcontroller that the pin connected to the forward drive button is an input pin that receives data. Successive commands carry the respective information for the remaining microcontroller pins. Command *Wire.begin* connects the master microcontroller to the I²C bus. Command *ControlMode* calls a function which describes the motor control mode selected by the user. The control mode is selected by the operator with the use of left or right turn switch. The left turn switch activates the unipolar mode, and the right turn switch activates the bipolar mode. Function codes are presented in Figure 3. The *while* command is a loop that checks the expression inside the parentheses. When the expression is true, the function inside the braces below the command is called. The absence of code inside braces denotes a void loop that will stop the program. The program waits until the expression inside the parentheses becomes false, in this case – until the right or left turn button is

```

16 void WyborSterowania() {
17 while( (digitalRead(prawo) == HIGH) && (digitalRead(lewo) == HIGH) )
18     { }
19     if(digitalRead(prawo) == LOW) {
20     Wire.beginTransmission(7);
21     Wire.write("b ");
22     Wire.endTransmission();
23
24     Wire.beginTransmission(8);
25     Wire.write("b ");
26     Wire.endTransmission();
27     while(digitalRead(prawo) == HIGH)
28         { } }
29     if(digitalRead(lewo) == LOW) {
30     Wire.beginTransmission(7);
31     Wire.write("u ");
32     Wire.endTransmission();
33
34     Wire.beginTransmission(8);
35     Wire.write("u ");
36     Wire.endTransmission();
37     while(digitalRead(lewo) == HIGH)
38         { } }
39 }

```

Fig. 3. Code for the master microcontroller – selection of motor control mode

pressed. Commands *if (digitalRead(right)==LOW)* and *if (digitalRead(left)==LOW)* are executed when the corresponding expressions are true.

For example, when the left turn button is pressed, the second *if* statement becomes true and information is transmitted to slave microcontrollers. Command *Wire.beginTransmission(7)* initiates communication with device 7 connected to the I²C bus. Command *Wire.write("bipolar")* sends data to an external device. In this case, the transmitted information is the word *bipolar* which denotes the selected motor control mode. Command *Wire.endTransmission()* ends the data transfer. Each command is repeated twice because data are sent to two microcontrollers – 7 and 8. The *while* loop after the *Communication* command makes the program wait until the user releases the button.

The code defines the direction of motor rotation. The *if* statement is called when the user presses the forward drive button (Fig. 4). The *Communication* function is called to send information to external microcontrollers. In the parentheses, 7 is the address of the receiving device, and 1 is the direction of motor rotation. The code for reverse drive (Fig. 5) and braking (Fig. 6) is similar.

```

80  if(digitalRead(przod)==LOW) {
81  Komunikacja(7,1);
82  Komunikacja(8,1);
83  while(digitalRead(przod)==LOW)
84  {      } }

```

Fig. 4. Code for the master microcontroller – forward drive

```

87  if(digitalRead(tyl)==LOW) {
88  Komunikacja(7,2);
89  Komunikacja(8,2);
90  while(digitalRead(tyl)==LOW)
91  {      } }

```

Fig. 5. Code for the master microcontroller – reverse drive

```

102 if(digitalRead(hamulec)==LOW)
103 {
104     KomunikacjaZnak(7,"h ");
105     KomunikacjaZnak(8,"h ");
106
107     while(digitalRead(hamulec)==LOW)
108     {      }
109     KomunikacjaZnak(7,"q ");
110     KomunikacjaZnak(8,"q ");
111 }

```

Fig. 6. Code for the master microcontroller – braking

The code for reverse drive and braking differs only in the data transmitted by the bus and the functions that are called by different buttons on the user console.

The microcontroller controls motor speed through the potentiometer on the user console. The code checks the value at the analog input connected to the potentiometer (Fig. 7).

```

65   predkoscAktualna = analogRead(potencjometr);
66   predkoscAktualna = map(predkoscAktualna, 0, 1023, 3, 255);
67
68   if(predkoscAktualna != predkoscPoprzednia)
69   {
70       predkoscPoprzednia = predkoscAktualna;
71
72       Komunikacja(7,predkoscAktualna);
73       Komunikacja(8,predkoscAktualna);
74   }

```

Fig. 7. Code for the master microcontroller – speed control

Values in the range of 0-1023 are stored in the *currentSpeed* variable. In the next step, the values are converted by the map function to the range of 3-255. The *if* statement checks potentiometer value. If potentiometer value has changed, the respective function is called to transmit information about motor speed to slave microcontrollers.

If the user wants to turn the vehicle and presses the left turn button, the motor speed value that is transmitted to the right motor controller is halved. As a result, the left motor turns at half the speed of the right motor, which causes the vehicle to turn in a given direction. The left turn code is presented in Figure 8, and the right turn code is presented in Figure 9.

```

125   if(digitalRead(lewo)==LOW)
126   {
127       Komunikacja(7,predkoscAktualna/2);
128       while(digitalRead(lewo)==LOW)

```

Fig. 8. Code for the master microcontroller – left turn

```

116   if(digitalRead(prawo)==LOW)
117   {
118       Komunikacja(8,predkoscAktualna/2);
119       while(digitalRead(prawo)==LOW)

```

Fig. 9. Code for the master microcontroller – right turn

The information sent by the master microcontroller to slave microcontrollers is composed of values in the range of 0 to 255 and ASCII characters. Each value and character carries specific information:

- 1 – forward drive,
- 2 – reverse drive,
- 3-255 – motor speed,
- 'h' – engage brake,
- 'q' – release brake,
- 'u' – unipolar motor control,
- 'b' – bipolar motor control.

Code for slave microcontrollers

The code for slave microcontrollers that drive motors contains functions responsible for:

- switching transistors in a desired commutation sequence at the corresponding pulse width modulation (PWM) values,
- defining rotor position,
- receiving information about operating parameters from the master microcontroller.

Electronic commutation

The main purpose of a slave microcontroller is to replace a mechanical commutator with an electronic commutator. Transistors are switched in a given commutation sequence to pass current through motor windings and to set the rotor in motion. The commutation sequences for transistor switches are presented in Table 1.

Table 1

Commutation sequences for transistor switches
when the motor turns right (clockwise)

	1	2	3	4	5	6
AH	1	0	0	0	0	1
BH	0	1	1	0	0	0
CH	0	0	0	1	1	0
AL	0	0	1	1	0	0
BL	0	0	0	0	1	1
CL	1	1	0	0	0	0

Microprocessor outputs AH, BH and CH supply upper transistor switches. Microprocessor outputs AL, BL and CL supply lower transistor switches. Numbers 1 to 6 in the top row of the table represent commutation steps. Two transistors are excited in each step. The commutation sequence has to be reversed to turn the motor in the left (counterclockwise) direction. The code for the function that switches transistors is presented in Figure 10.

```

16 void NastepnyKrokKomutacji(int krok) {
17     switch(krok) {
18         case 0:  AH_BL(); break;
19         case 1:  AH_CL(); break;
20         case 2:  BH_CL(); break;
21         case 3:  BH_AL(); break;
22         case 4:  CH_AL(); break;
23         case 5:  CH_BL(); break;
24     }
25 }

```

Fig. 10. Code for slave microcontrollers – function for switching transistors

The function initiates one of the six commutation steps to pass current through windings. For example, step 0 calls function AH_BL () which powers the upper transistor A and the lower transistor B.

The function that powers transistors sets the value of microcontroller outputs to 9 and 6 to send a PWM signal to the transistor driver (Fig. 11). Pulses are generated by DC to AC inverters and by frequency converters. Pulse width is modulated by switching transistors on and off. This approach supports easy and high-precision control.

```

84 void AH_BL() {
85     analogWrite(9, Pwm1);
86     analogWrite(6, Pwm2);
87     analogWrite(10, 0);
88     analogWrite(11, 0);
89     analogWrite(3, 0);
90     analogWrite(5, 0);
91 }

```

Fig. 11. Code for slave microcontrollers – function that sets PWM value at microcontroller outputs

Determining rotor position in a BLDC motor

Information about rotor position is required for the correct operation of a brushless motor. The controller is equipped with a rotor position sensor. Hall effect sensors mounted on coil windings send information about rotor position to the microcontroller by outputting a value of 0 or 1.

The combination of values output by three sensors describes rotor position (Fig. 12). When rotor position has been detected and the time of the next commutation step has been determined, the program calls a function that activates the next transistor pair.

```
194     stanHallA = digitalRead(hallA);
195     stanHallB = digitalRead(hallB);
196     stanHallC = digitalRead(hallC);
```

Fig. 12. Code for slave microcontrollers – values output by Hall effect sensors

The code that checks the combination of values output by Hall effect sensors is presented in Figure 13. If sensors C and A output 1, the *outputHall* variable is assigned a value that corresponds to the next commutation step.

```
42 void wykrywaniePolozeniaPrawo() {
43     if ((stanHallC == 1) && (stanHallB == 0) && (stanHallA == 1)) {
44         stan = 0;
45     }
46     if ((stanHallC == 0) && (stanHallB == 0) && (stanHallA == 1)) {
47         stan = 1;
48     }
49     if ((stanHallC == 0) && (stanHallB == 1) && (stanHallA == 1)) {
50         stan = 2;
51     }
52     if ((stanHallC == 0) && (stanHallB == 1) && (stanHallA == 0)) {
53         stan = 3;
54     }
55     if ((stanHallC == 1) && (stanHallB == 1) && (stanHallA == 0)) {
56         stan = 4;
57     }
58     if ((stanHallC == 1) && (stanHallB == 0) && (stanHallA == 0)) {
59         stan = 5;
60 }}
```

Fig. 13. Code for slave microcontrollers – detection of rotor position

I²C communication and motor control

The information about motor speed and direction is transmitted by the master microcontroller via the I²C data bus. The relevant data is sent in the form of values and ASCII characters. The slave microcontroller receives data and calls the corresponding functions. The code that enables slave microcontrollers to receive data is presented in Figure 14.

```

27 void odbierzInformacje(int howMany) {
28   while (1 < Wire.available()) {
29     c = Wire.read();
30     if(c == 'u') {metoda=1; } // metoda true unipolarna
31     if(c == 'b') {metoda=2; } // metoda false bipolarna
32     if(c == 'h') {hamulecWlacz();}
33     if(c== 'q') {hamulecWylacz(); c='r';}
34   }
35   x = Wire.read();
36   if(x==1) {kierunekObrotow=2;} //lewo
37   if(x==2) {kierunekObrotow=1; } // prawo
38   if(x>=3) {predkosc=x; predkosc=map(predkosc,3,255,10000,1000);}
39 }

```

Fig. 14. Code for slave microcontrollers – receiving data transmitted by the I²C bus

The *receiveInformation* function is called when information is received. The transmitted information is composed of ASCII characters such as *u*, *b*, *h* and *q*, and values in the range of 0 to 255. The *if* statement in the function code defines the direction of motor rotation. The unipolar or bipolar control mode has to be selected when the controller is activated. Character *u* denotes the unipolar mode, and character *b* denotes the bipolar mode. The direction of motor rotation which determines the direction of drive is determined in the next step. Value 1 indicates that the motor is moving in the right (clockwise) direction, and value 2 indicates that the motor is moving in the left (counterclockwise) direction. Values higher or equal to 3 denote motor speed. The higher the value, the faster the commutation sequence. Character *h* denotes electric braking, and the microcontroller activates two motor windings until character *q* is received.

Summary

The designed controller for brushless DC motors has been patented (SYROKA, KRAJEWSKI 2019) for use in commercial applications. The device can be applied in electric vehicles for controlling BLDC motors mounted in wheels. It was

developed as part of a research project at the University of Warmia and Mazury in Olsztyn (Books – Digital Control, SYROKA 2019) dedicated to the construction of electric vehicles and electric drives that rely on renewable sources of energy.

References

- ÅSTROM K.J., MURRAY R.M. 2006. *An Introduction for Scientists and Engineers*. Feedback Systems. Princeton University Press, Princeton, Oxford.
- BOLTON W. 2006. *Programmable Logic Controllers*. Elsevier, Amsterdam.
- BUSO S., MATTAVELLI P. 2006. *Digital Control in Power Electronics*. Morgan & Claypool, Publisher, San Rafael, CA.
- CHEN C.-T. 1991. *Analog and Digital Control system Design: Transfer Function, State Space, and Algebraic Methods*. Saunders College Publishing, Philadelphia, Pennsylvania.
- DENTON T. 2016. *Electric and Hybrid Vehicles*. Routledge, London.
- DORF R.C., BISHOP R.H. 2008. *Modern Control System Solution Manual*. Prentice Hall, Upper Saddle River, New Jersey.
- EMADI A., ALIREZA K., ZHONG N., YOUNG J.L. 2009. *Integrated Power Electronic Converters and Digital Control*. CRC Press LLC, Boca Raton, Florida.
- EMADI A., EHSANI M., MILLER J.M. 2004. *Power Systems, Land, Sea, Air, and Space Vehicles*. Marcel Dekker, New York.
- FADALI S. 2009. *Digital Control Engineering, Analysis and Design*. Elsevier, Amsterdam.
- FEUER A., GOODWIN G.C. 1996. *Sampling in Digital Signal Processing and Control*. Brikhauser, Bazylea.
- GABOR R., KOWOL M., KOŁODZIEJ J., KMIĘCIK S., MYNAREK P. 2019. *Switchable reluctance motor, especially for the bicycle*. Patent No 231882.
- GLINKA T., FRECHOWICZ A. 2007. *Brushless DC motor speed control system*. Patent No.P195447.
- IQBAL H. 2003. *Electric and Hybrid Vehicles, Design Fundamentals*. CRC Press LLC, Boca Raton, Florida.
- JONGSEONG J., WONTAE J. 2019. *Method of controlling constant current of brushless dc motor and controller of brushless dc motor using the same*. United States Patent Application Publication, US2018323736 (A1).
- KHAJEPOUR A., FALLAH S., GOODARZI A. 2014. *Electric and Hybrid Vehicles Technologies, Modeling and Control: a Mechatronic Approach*. John Wiley & Sons Ltd, Hoboken, New Jersey.
- KOJIMA, N., ANNAKA T. 2019. *Motor control apparatus and motor unit*. United States Patent Application Publication, US2019047517 (A1).
- KOLANO K. 2020. *Method for measuring the angular position of the shaft of a brushless DC motor with shaft position sensors*. Patent No.P235653.
- LANDAU I.D., ZITO G. 2006. *Digital Control Systems Design, Identification and Implementation*. Springer, Berlin.
- LUECKE J. 2005. *Analog and Digital Circuits for Electronic Control System Applications Using the TI MSP430 Microcontroller*. Elsevier, Amsterdam.
- MI CH., MASRUR M.A., GAO D.W. 2011. *Hybrid Electric Vehicles Principles and Applications with Practical Perspectives*. John Wiley & Sons Ltd, Hoboken, New Jersey.
- MOUDGALYA K.M. 2007. *Digital Control*. John Wiley & Sons Ltd., Hoboken.
- MURRAY R.M., LI Z., SHANKAR SASTRY S. 1994. *A Mathematical Introduction to Robotic Manipulation*. CRC Press LLC, Boca Raton, Florida.
- OGATA K. 1995. *Discrete Time Control Systems*. Prentice-Hall, Upper Saddle River, New Jersey.
- PISTOIA G. 2010. *Electric and Hybrid Vehicles Power Sources, Models, Sustainability, Infrastructure and the Market*. Elsevier, Amsterdam.

- SIKORA A., ZIELONKA A. 2011. *Power supply system for a BLDC motor*. Patent No. P.394971.
- ŚLUSAREK B., PRZYBYLSKI M., GAWRYŚ P. 2014. *Hall effect sensor of the shaft position of the brushless DC motor*. Patent No.P218476.
- SOYLU S. 2011. *Electric Vehicles – the Benefits and Barriers*. IntechOpen, London.
- STARR G.P. 2006. *Introduction to Applied Digital Control*. Springer, Berlin.
- STEVIC Z. 2012. *New Generation of Electric Vehicles*. IntechOpen, London.
- SYROKA Z., KRAJEWSKI K. 2019. *Controller for brushless DC motors*. Patent No. P431380. Filing date: 4 October 2019.
- SYROKA Z.W. 2019. *Electric Vehicles – Digital Control*. Scholars' Press, Riga.
- WILLIAMSON S.S. 2013. *Energy Management Strategies for Electric and Plug-in Hybrid Electric Vehicles*. Springer, Berlin.



STRUCTURAL ANALYSIS OF FE-AL COATINGS APPLIED BY GAS DETONATION SPRAYING

Tomasz Chrostek

ORCID: 0000-0002-6516-8192

Department of Materials and Machine Technology
University of Warmia and Mazury in Olsztyn

Received 10 November 2020, accepted 3 December 2020, available online 4 December 2020.

Key words: Gas Detonation Spraying, intermetallic FeAl alloys.

Abstract

The article analyzes the formation of oxide phases in the structure of intermetallic FeAl coatings applied by gas detonation spraying (GDS). The structural properties of powder charge particles and FeAl coating formed during GDS were determined. The effect of the GDS process on phase changes in FeAl coating applied under controlled conditions was examined. The results indicate that at specific process parameters, FeAl powder particles are strongly oxidized in a hot stream of gases produced during supersonic combustion. Powder particles undergo very strong plastic deformation during the process, and the resulting multiphase coating contains oxide phases that form thin membranes along grain boundaries.

The results of structural analyses and microanalyses of chemical composition (SEM/EDS) and phase composition (XRD) indicate that strongly heated FeAl particles undergo surface oxidation during GDS and are transformed into grains (splats) when they collide with a steel substrate. The produced FeAl coating has a multi-layered and multi-phase structure characteristic of the sprayed material, and it contains thin oxide layers, mainly Al_2O_3 .

Introduction

Intermetallic materials have numerous practical applications due to their unique properties (NIEWIELSKI, JABŁOŃSKA 2007). FeAl alloys can be applied by the gas detonation spraying (GDS) method to form protective coatings (HEJWOWSKI 2013). The GDS method is characterized by supersonic flow of the two-phase (gas-powder) metallizing stream. Strongly heated powder particles have very high kinetic energy when they collide with the substrate (ASSADI et al. 2016, FIKUS et al. 2019, LIU et al. 2007). FeAl coatings produced in the GDS process have many advantages, including considerable resistance to high temperature in chemically aggressive environments and very high resistance to tribological wear (BOJAR et al. 2002).

The thermal energy of gaseous detonation products directly influences the metallurgical quality of sprayed FeAl coatings (CHROSTEK et al. 2019). Research has demonstrated that even minor changes in a single parameter of the GDS process, including the fuel-oxidizer ratio, the amount of gas transporting powder particles, spraying frequency, spraying distance, and powder position inside the barrel at the time of detonation, significantly affect the kinetic and thermal energy of the stream of gaseous detonation products, which influences the quality of the sprayed coatings (NIKOLAEV et al. 2003, SADEGHIMERESHT et al. 2017).

The rate of chemical reactions in strong shockwaves is extremely high during thermal spraying. These reactions produce free radicals which significantly affect the oxidation of strongly heated powder particles. Powder particles undergo partial surface melting, and their oxidation is further exacerbated during transport by gaseous detonation products (SENDEROWSKI et al. 2016).

The aim of this study was to compare the structural parameters of FeAl powder and FeAl protective coating applied by the GDS method. The results of the comparison were used to evaluate the degree of oxidation and phase stability of intermetallic coating sprayed with a detonation gun.

Materials and Methods

The analyzed intermetallic protective coating was produced by GDS of powder composed of a mixture of Fe and Al elemental powders with a composition of Fe₄₀Al_{0.05}Zr-50 ppm B, at%. The powder was manufactured by LERMPS-UTBM with the use of the Vacuum Inert Gas Atomization (VIGA) method. The substrate was a sample of 15HM (13CrMo4-5) boiler steel measuring 50×50×5 mm which was blasted with alumina directly before spraying. Surface roughness after sandblasting the substrate was Ra = 18.98 μm. The coating in the form of circular deposit was sprayed by placing the substrate material

in a fixed position relative to the barrel of the detonation gun operating at a frequency of 6.66 Hz (Fig. 1). The barrel had a length of 1,090 mm, and it was positioned at a distance of $L = 110$ mm from the sprayed substrate. The powder with $5 \div 40 \mu\text{m}$ particle size was loaded into the gun, and it was located at a distance of 412.5 mm from the barrel outlet at the time of detonation (powder injection position – PIP). Spraying parameters, the composition of the explosive detonation mix, and the flow rate of powder-transporting air are presented in Table 1. The FeAl coating was sprayed with the use of the Perun-S detonation gun at the Department of Protective Coatings, E.O. Paton Electric Welding Institute of the Ukrainian National Academy of Sciences. The variations in the geometric dimensions of the sprayed FeAl coating after 100 gun shots were determined with a PG10 profilometer (Fig. 1b).

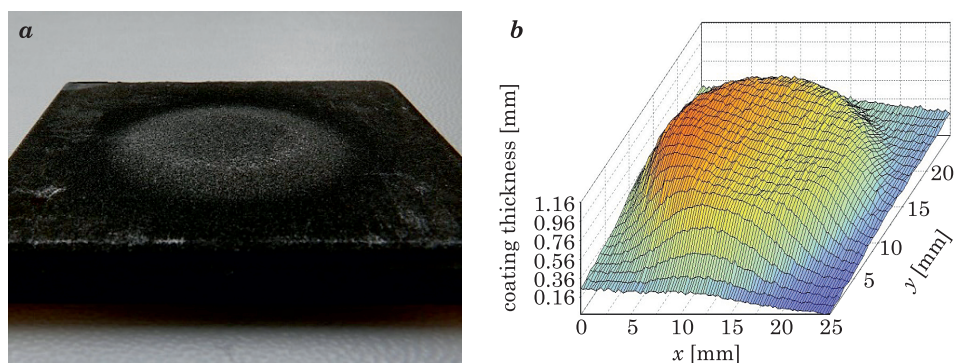


Fig. 1. FeAl coating sprayed onto 15HM (13CrMo4-5) boiler steel under GDS conditions specified in Table 1: *a* – macro image, *b* – 3D geometric dimensions of the FeAl coating after 100 gun shots

Table 1

GDS spraying parameters			
Fe40Al0,05Zr at%+50 ppm B powder Particle size distribution (granulation) 5-40 μm			
Spraying frequency f [Hz]	6.66	powder transporting gas – air	0.4 m^3/h
		oxygen-fuel mixture	C_3H_8 – 0.45 m^3/h O_2 – 1.52 m^3/h air (as diluter gas)– 0.65 m^3/h
Spraying distance L [mm]	barrel length l [mm]	powder injection position* PIP [mm]	thickness of the FeAl coating after 100 gun shots H [mm]
110	1,090	412.5	0.68 – 0.75

* Powder injection position – powder position inside the barrel at the time of detonation

Structural analyses, including analyses of the morphology, chemical composition and phase composition of the original powder particles (as supplied by the manufacturer) and the produced FeAl coating, were performed under a scanning electron microscope with energy-dispersive X-ray spectroscopy (SEM/EDS) and X-ray diffraction (XRD).

A point analysis and an analysis of the surface distribution of elemental powder components and the sprayed FeAl coating were conducted under the Quanta 3D FEG Dual Beam scanning electron microscope with a secondary electron (SE) detector which supports the acquisition of high-quality topographic images, and a backscattered electron (BSE) detector which supports the acquisition of topographic images and analyses of differences in chemical composition. Chemical composition was analyzed by SEM/EDS in microregions with the use of the EDAX Genesis Spectrum v.6.29 analyzer. The Quanta 3D FEG Dual Beam microscope relies on a focused coherent electron beam for analyzing the chemical composition of microregions with a diameter of 0.5 μm (for point analysis) and an area of 10 mm^2 (for mapping).

X-ray diffraction analysis was conducted with the Rigaku Ultima IV diffractometer with focused monochromatic CoK_α radiation and a spectral wavelength of $\lambda = 0.178897$ nm. CoK_α filtering was applied, and the operating parameters of the radiation lamp were set at 40 kV/40 mA. Data were collected within the angular range of 20° to 120° at a scanning speed of 1 mm/min.

Results and Discussion

The size, morphology and phase composition of powder particles significantly influence the metallurgical quality of coatings produced by thermal spraying, including GDS. These parameters considerably affect the thermophysical properties of powders and, consequently, the performance of the produced protective coatings.

A structural analysis (VIGA) of the original FeAl powder (as supplied by the manufacturer) revealed considerable differences in particle size. Powder particles were spherical in shape regardless of their size (Fig. 2a). The observations of metallographic specimens of FeAl powder produced with the VIGA method revealed variously shaped and sized pores in differently sized powder particles (Fig. 2). Powders are produced in the liquid phase of FeAl alloy melting in a vacuum induction furnace, and they are sprayed with high-purity argon to prevent oxidation. Pores are probably formed under the influence of the argon stream and during the shrinkage of a solidifying alloy when gas bubbles inside powder particles create empty spaces.

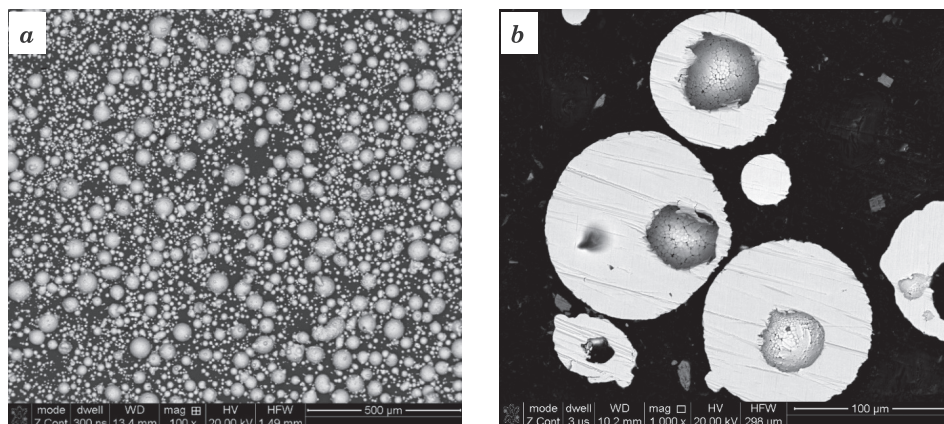


Fig. 2. Original FeAl powder (as supplied by the manufacturer) (VIGA) in the SEM/EDS analysis: *a* – differences in particle size, *b* – porous FeAl powder particles at the cross-section of the prepared metallographic specimen

The SEM/EDS surface microanalysis conducted at the cross-section of the original FeAl powder particles (as supplied by the manufacturer) demonstrated that their chemical composition corresponds to the FeAl phase with estimated 44% Al content and no oxygen (Fig. 3). This result indicates that argon effectively prevents the oxidation of sprayed FeAl particles made of inductively melted FeAl alloy in the VIGA process.

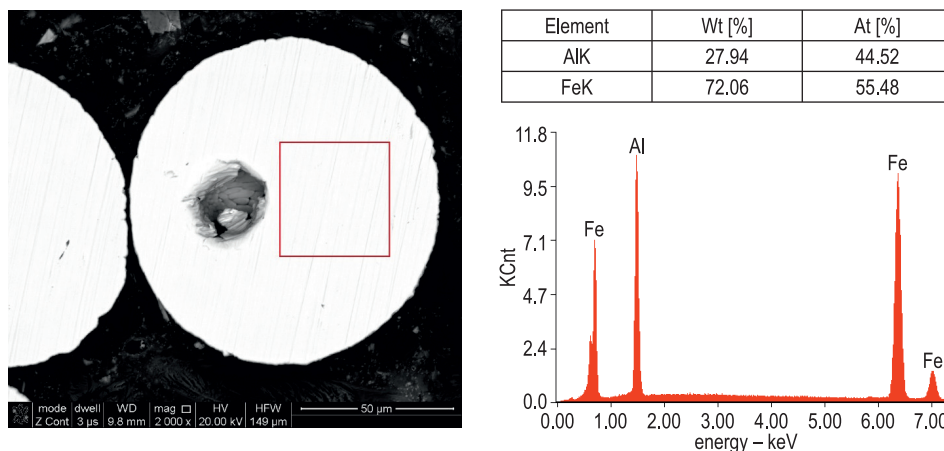


Fig. 3. Surface microanalysis of the chemical composition of original FeAl powder particles (as supplied by the manufacturer) with a marked region of SEM/EDS analysis

The XRD analysis of phase composition revealed the single-phase structure of FeAl powder particles with a characteristic reflection {100} of the B2 superstructure, which confirms that the original FeAl powder particles (as supplied by the manufacturer) were not oxidized (Fig. 4). A very small half-width of X-ray reflections with highly intense peaks, which is characteristic of a given family of FeAl phase lattice planes within a specified range of Bragg angles, can be attributed to the homogeneous chemical composition of individual powder particles and very low residual stress values. The above preserves the structural integrity of the crystal structure of the FeAl phase, which is a secondary solid solution of Al in Fe(*a*) and constitutes the basis of the single-phase powder without oxide phases.

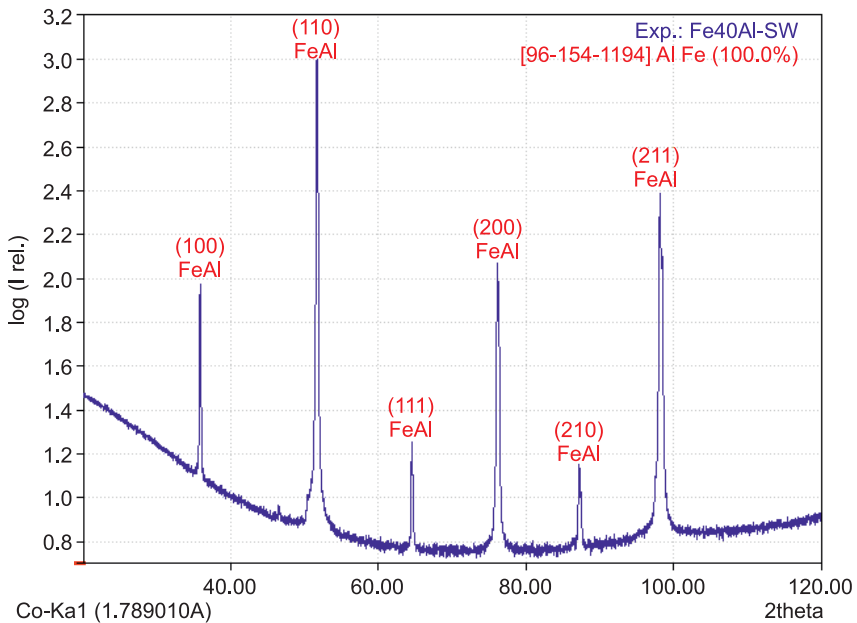


Fig. 4. XRD phase composition analysis of the original FeAl powder (as supplied by the manufacturer) produced in the VIGA process

Gaseous detonation products which create a two-phase metallizing stream with the FeAl powder are characterized by high kinetic energy and very high thermal energy during detonation spraying of FeAl coatings. These gases lead to the volumetric deformation of powder particles which are heated to near-melting temperature, and the formation of protective coatings when powder particles collide with the steel substrate material.

A review of the literature indicates that thermal and kinetic phenomena during detonation can be controlled by modifying heating and spraying parameters,

including fuel type, the fuel-oxidizer ratio, PIP in the barrel at the time of detonation, spraying frequency and distance (SENDEROWSKI 2015). The heating of powder particles can be controlled by adapting GDS conditions to the type of coating material, including its melting temperature, thermal and physical parameters, and the size and morphology of powder particles (ULIANITSKY et al. 2011).

The structural analysis of FeAl coating revealed significant changes in the physicochemical and mechanical properties of FeAl powder particles sprayed with a frequency of 6.66 Hz (Fig. 5). The observed changes resulted from particle heating and their plastic deformation.

The particle deformation analysis and the SEM/EDS microanalysis of the surface of FeAl coating revealed partial melting of powder particles in selected regions (Fig. 5). Particle melting leads to very strong oxidation of diffused aluminum and the formation of oxide phases on the surface of partially melted FeAl particles that form dark grains with a varied morphology in SEM/BSE images (Fig. 5). The SEM/EDS point microanalysis confirmed considerable variations in the chemical composition of grains in the FeAl coating, where aluminum content was estimated at 4-45 at% and oxygen content was determined

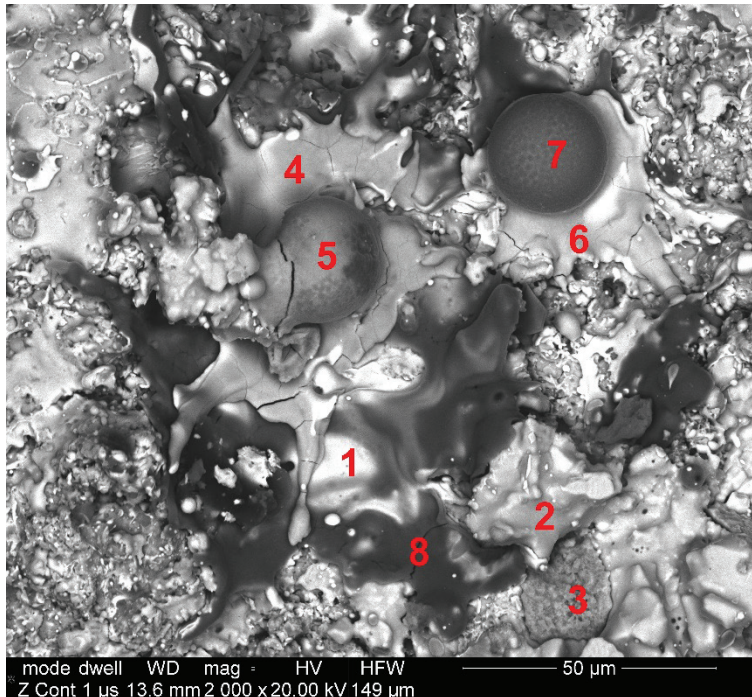


Fig. 5. SEM/EDS microanalysis of the chemical composition of FeAl coating sprayed with a detonation gun

at up to 52 at% in the region of dark grains (Fig. 5, Table 2). These results clearly indicate that the intermetallic phases of FeAl alloys differ considerably in aluminum content and are characterized by a high content of oxygen which forms complex aluminum oxides Al_2O_3 and oxide spinels.

Table 2

Results of the SEM/EDS point microanalysis of the chemical composition of grain microregions on the surface of FeAl coating (GDS) presented in the SEM/BSE image in Figure 5

Phase	Element	Wt%	At%	Phase	Element	Wt%	At%
1	Al	4.78	8.84	5	Al	18.79	20.24
	Fe	92.51	82.69		Fe	52.29	27.22
	O	2.71	8.47		O	28.92	52.55
2	Al	27.65	42.47	6	Al	3.83	4.88
	Fe	70.27	52.14		Fe	72.56	44.55
	O	2.08	5.39		O	23.61	50.57
3	Al	19.47	22.32	7	Al	32.23	32.04
	Fe	56.57	31.34		Fe	38.19	18.35
	O	23.96	46.34		O	29.59	49.61
4	Al	8.06	10.93	8	Al	52.86	45.04
	Fe	74.35	48.77		Fe	12.47	5.14
	O	17.60	40.29		O	34.67	49.82

The SEM/EDS structural analysis of FeAl coating (GDS) performed at the cross-section of the metallographic specimen revealed lamellar grains with a multi-phase structure and varied chemical composition. In the images acquired with the use of the BSE detector, differences in the chemical composition of different regions on the surface of FeAl coating were presented in shades of gray (Fig. 6a).

The observed variations in the chemical composition of plastically deformed FeAl powder particles (with a single-phase structure in the original state) can be attributed to chemical reactions that take place in the stream of gaseous detonation products and the *in situ* formation of oxide phases in the form of oxide membranes in the GDS process (dark layers in Fig. 6a). When analyzing the oxidation of the FeAl coating produced by the GDS method, special attention should be paid to the preferential sites for the formation of oxide phases. These sites represent partially melted FeAl powder particles where thin oxide layers are formed, undergoing strong non-dilatational strain when the particles collide with the substrate material in a supersonic detonation wave. The produced coating has a mosaic structure (Fig. 6). Aluminum is depleted, and the intermetallic

Fe_3Al phase and the secondary Al solution in Fe_α are formed in regions adjacent to strongly oxidized phases with a chemical composition of Al_2O_3 , $\text{Fe}(\text{Al}_2\text{O}_4)$ and Fe_3O_4 .

The content of alloy elements and oxygen mapped in the SEM/EDS microanalysis of chemical composition at the cross-section of FeAl coating (GDS) is presented in Table 3.

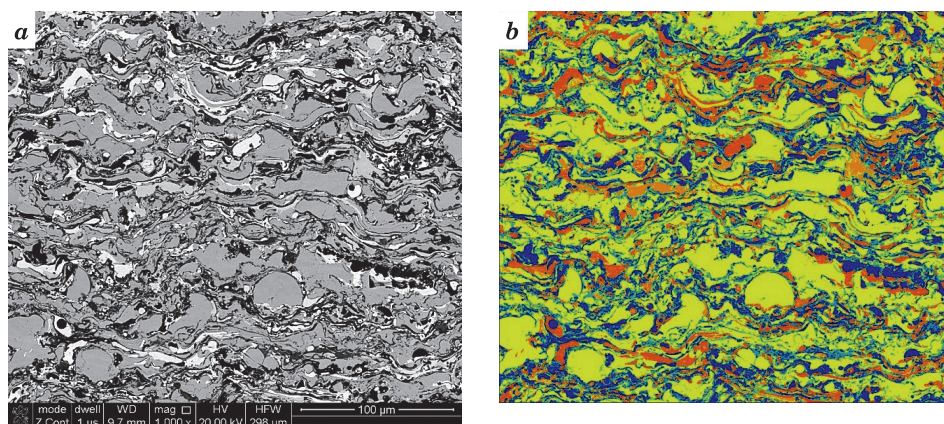


Fig. 6. SEM/BSE image of the multi-phase structure of FeAl coating produced in the GDS process (a); SEM/EDS surface microanalysis of the chemical composition of alloy elements with oxygen (b)

Table 3

Content of alloy elements and oxygen mapped in the SEM/EDS microanalysis of chemical composition at the cross-section of FeAl coating (GDS) (Fig. 6b)

Analyzed region on coating surface		Content of alloy elements [% at]			Probable phase
Color	content [% vol.]	Fe	Al	O	
Blue	13	0.91	47.66	51.43	Al_2O_3 phase
Light blue	8.58	22.00	34.33	43.66	$\text{Fe}(\text{Al}_2\text{O}_4)$ phase
Green	14.62	49.05	11.36	39.59	FeO , Fe_2O_3 , Fe_3O_4 oxide phases
Yellow	47.46	55.72	40.61	3.68	weakly oxidized FeAl phase
Orange	9.41	76.44	18.88	4.68	weakly oxidized Fe_3Al phase
Red	6.92	92.53	1.01	6.37	oxidized ferrite

The SEM/EDS surface microanalysis of the chemical composition of the FeAl coating revealed a high degree of oxidation (Fig. 6 and Tab. 3). The FeAl phase (marked in yellow) of the FeAl coating (GDS) was predominant (approx. 48% vol.), and it was composed of strongly plastically deformed splats (Fig. 6b). The proportion of oxide phases (blue, light blue and green in Fig. 6b) on the

surface of strongly deformed powder particles was also high and significant, and it was estimated at 36% vol. of the FeAl coating (GDS).

Thin oxide phase membranes along grain boundaries in the intermetallic FeAl coating did not cause granular delamination in the form of microcracks, which was potentially possible due to differences in the values of the linear coefficients of thermal expansion for the FeAl phase and ceramic oxides. The SEM/EDS analysis revealed that the Fe_3Al phase (orange), which was depleted of aluminum due to the formation of oxide phases, accounted for around 10% vol. of the FeAl coating and was created directly in the region of oxide phase formation (Fig. 6 and Tab. 3).

The X-ray diffraction analysis of FeAl coating (GDS) confirmed that the FeAl phase is the main structural component that is inherited from FeAl powder (VIGA). The analysis also confirmed the presence of the Fe_3Al phase and the following oxide phases: aluminum oxide – Al_2O_3 , spinel – $\text{Fe}(\text{Al}_2\text{O}_4)$, magnetite – Fe_3O_4 and ferrous oxide – FeO (Fig. 7).

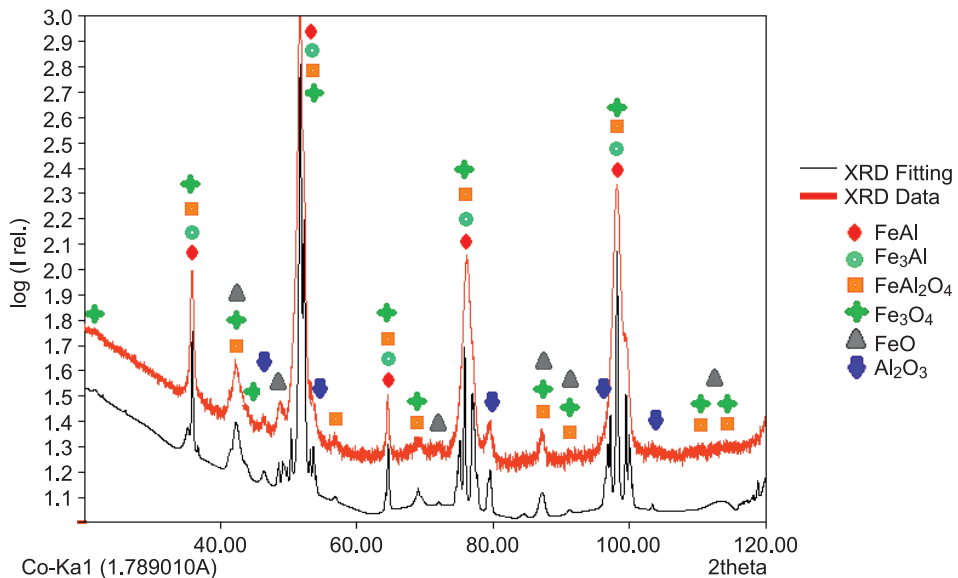


Fig. 7. XRD analysis of the phase composition of FeAl coating sprayed with a detonation gun

A comparison of the XRD image of the FeAl coating (GDS) (Fig. 7) with the XRD image of the original FeAl powder (Fig. 4) indicates that an increase in the half-width of FeAl coating reflections and a decrease in reflection intensity probably resulted from the high dispersivity of Al_2O_3 phases and oxide spinels identified as $\text{Fe}(\text{Al}_2\text{O}_4)$. The oxide phases identified in XRD analysis contribute

to the formation of pseudo-composite coating and increase residual stress in the structure of the intermetallic FeAl coating, which also widens the reflections of diffraction peaks.

The behavior of the superstructure peak {100} indicates that the sprayed coating is based on the FeAl (B2) phase which has a less ordered structure and contains the aluminum-deficient Fe₃Al phase without superstructure reflection (Fig. 7).

Conclusions

During the GDS of intermetallic FeAl coating with the use of single-phase FeAl alloy powder produced by the VIGA method, the detonation wave and gaseous detonation products lead to the oxidation of particle surfaces and the formation of oxide membranes which are an integral part of coatings with a layered structure. The supersonic metallizing stream causes strong volumetric deformation of powder particles when they collide with the substrate material. Thin oxide membranes are formed along the boundary of strongly flattened grains without impairing their cohesiveness. Aluminum is depleted in the region where oxide phases are formed, and a solid solution of the secondary Fe₃Al phase is formed in microregions.

The pseudo-composite structure of intermetallic FeAl coating with oxide phases is characterized by a less ordered structure and higher residual stress which is exacerbated by dispersive oxide phases. Residual stress generated during GDS does not cause microcracks in the multi-phase structure of FeAl coatings containing ceramic oxides which stabilize the structure during high-temperature heating, including in aggressive corrosive environments.

References

- ASSADI H., KREYE H., GARTNER F., KLASSEN T. 2016. *Cold spraying e A materials perspective*. Acta Materialia, 116: 382-407.
- BOJAR Z., SENDEROWSKI C., DUREJKO T. 2002. *Structure and tribological properties of FeAl-based intermetallic coatings sprayed on steel substrate*. International Journal of Applied Mechanics and Engineering, 7: 335-340.
- CHROSTEK T., BRAMOWICZ M., RYCHLIK K., WOJTKOWIAK A., SENDEROWSKI C. 2019. *Influence of gas detonation spraying parameters on the geometrical structure of FeAl intermetallic protective coating*. Technical Sciences, 22(3): 249-262.
- FIKUS B., SENDEROWSKI C., PANAS A.J. 2019. *Modeling of Dynamics and Thermal History of Fe40Al Intermetallic Powder Particles Under Gas Detonation Spraying Using Propane-Air Mixture*. Journal of Thermal Spray Technology, 28(3): 346-358.
- HEJWOWSKI T. 2013. *Nowoczesne powłoki nakładane cieplnie odporne na zużycie ściernie i erozyjne*. Monografie – Politechnika Lubelska, Lublin.

- LIU S.-G., WU J.-M., ZHANG S.-C., RONG S.-J., LI Z.-Z. 2007. *High temperature erosion properties of arc-sprayed coatings using various cored wires containing Ti-Al intermetallics*. *Wear*, 262: 555-561.
- NIEWIELSKI G., JABŁOŃSKA M. 2007. *Charakterystyka i zastosowanie intermetalii z układu FeAl*. *Inżynieria Materiałowa*, 2: 43-47.
- NIKOLAEV YU.A., VASIL'EV A.A., UL'YANITSKII B.YU. 2003. *Gas Detonation and its Application in Engineering and Technologies (Review)*. *Combustion, Explosion and Shock Waves*, 39(4): 382-410.
- SADEGHIMERESHT E., MARKOCSAN N., NYLÉN P. 2017. *Microstructural characteristics and corrosion behavior of HVAF- and HVOF-sprayed Fe-based coatings*. *Surface & Coatings Technology*, 318: 365-373.
- SENDEROWSKI C. 2015. *Żelazowo-aluminiowe intermetaliczne systemy powłokowe uzyskiwane z naddźwiękowego strumienia metalicznego*. Bel Studio Sp. z o.o., Warszawa.
- SENDEROWSKI C., DUREJKO T., ZASADA D., NAPADLEK W., BOJAR Z. 2016. *Structure and properties of the FeAl (HVOF, HVAF, DGS) coating for power industry*. *Inżynieria Materiałowa*, 6(214): 283-288.
- ULIANITSKY V., SHTERTSER V., ZLOBIN S., SMUROV I. 2011. *Computer-controlled detonation spraying: from process fundamentals toward advanced applications*. *Journal of Thermal Spray Technology*, 20(4): 791-801.



INFLUENCE OF SELECTED ASPECTS OF THE TECHNICAL CONDITION OF MEANS OF TRANSPORT OPERATING IN WIELKOPOLSKA IN POLAND ON ROAD SAFETY

Piotr Gorzelanczyk

ORCID: 0000-0001-9662-400X

Stanislaw Staszic University of Applied Sciences in Pila

Received 10 October 2020, accepted 2 December 2020, available online 3 December 2020.

Key words: Technical condition of means of transport, road accidents, lighting, tires.

Abstract

The aim of the article is an attempt to determine whether the technical condition of vehicles in Wielkopolska has an impact on road traffic. For this purpose, the lighting of 20 passenger vehicles and tires in public transport and driving school cars in Wielkopolska were analysed. The lighting of the subject vehicles was organoleptically tested and their intensity and dipped beam were checked at the vehicle inspection station. In the case of five of the tested vehicles, the luminous intensity was at an unsatisfactory level. In the next step, the tires of 16 randomly selected buses were tested. Tread wear tests were discussed in the analysed buses and the influence of tread wear on tire exploitation was presented. For the tested buses, it is noteworthy that the tires were changed if the tread height was too low. In the last step of the research, the tires of a driving school truck were analysed. It was found that the wear of the tire is not even due to driving on a manoeuvring area. Based on the above tests, it can be concluded that the technical condition of road vehicles is important and affects their operation and safety.

Introduction

The technical condition of vehicles on roads is important in terms of safety. Each mode of transportation, if it is technically inefficient, may pose a significant threat to health or even life (AMBROŻUK, WESOŁOWSKI 2017, KUŁAKOWSKA, PATYK 2013).

In recent years, there has been a rapid development of motorisation, and this has caused an increase in the number of vehicles on Polish roads (Fig. 1). In the last 10 years, the number of registered cars in Poland increased by nearly 50%.

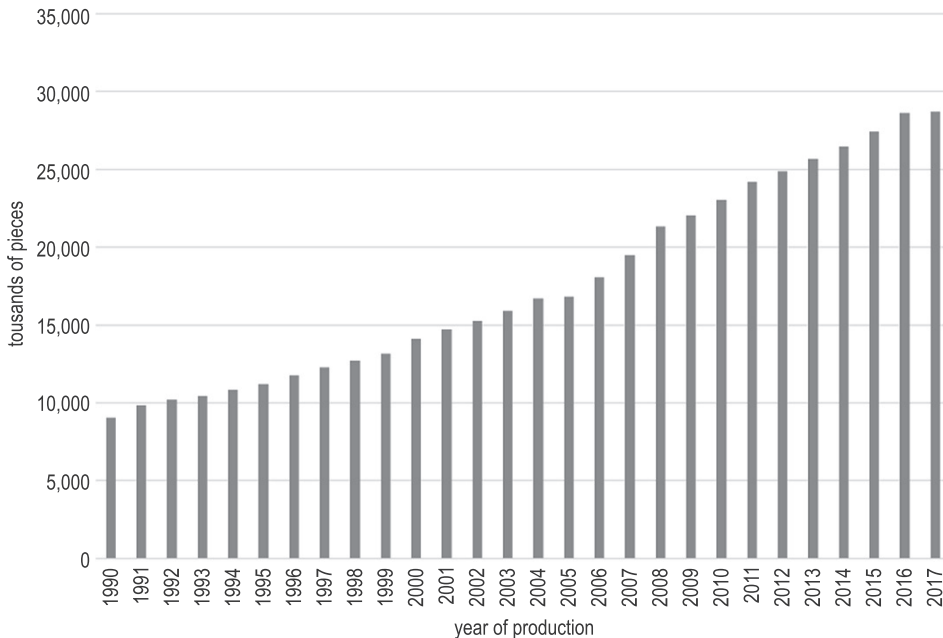


Fig. 1. The number of means of transport in 2001-2017

For this reason, the technical condition of vehicles traveling on the road is significant, affecting not only the safety of road users but also the environment and human health. Poor vehicle technical condition can lead to many accidents resulting in injuries and fatalities. At the turn of 2001-2016, as a result of poor technical condition, there were 1,795 accidents in which 208 people were killed and 2,344 people were injured (Polish Police 2018). These data are presented in Table 1.

The number of road accidents caused by the technical condition is less than 1% of all accidents, however, such cases do occur. Lighting defects in vehicles involved in road accidents in the analysed period amounted to 482, which accounts for

Table 1

Number of road accidents caused by the poor vehicle technical condition

Year	Number of accidents	Number of defects associated with lighting in vehicles involved in road accidents	Number of defects related to the condition of tires in vehicles involved in road accidents	Fatalities	Injuries
2001	19	1	3	2	26
2002	22	2	5	2	41
2003	16	2	1	1	22
2004	14	2	1	1	15
2005	11	2	5	2	16
2006	233	48	57	41	265
2007	114	61	28	21	140
2008	143	76	28	13	185
2009	101	42	21	8	147
2010	66	33	12	13	87
2011	80	43	13	5	97
2012	55	29	12	6	66
2013	53	26	16	6	63
2014	44	36	7	5	59
2015	41	35	7	10	41
2016	64	26	16	8	81
2001-2016	1,795	482	242	208	2,344

Source: Polish Police (2018).

27% of all accidents caused by the technical condition. Therefore, the technical condition of the tires caused 242 accidents in the analysed period. This accounts for 14% of all accidents caused by poor technical condition. For this reason, the article attempts to determine if the technical condition of selected aspects of vehicles in Wielkopolska has an impact on road safety.

Characteristics of vehicle lighting

Technological progress and road safety requirements force constant changes in the construction of car lights. Changing the style and constantly following recent trends also affects the appearance, design and the technology used in vehicle lighting. Road lights at the front of the vehicle have the greatest impact on traffic safety. These types of light sources include spotlights. Depending on the type, there are smooth or ribbed glass panes with a paraboloid or multi-parabolic

reflector. Currently found headlights are so-called combined reflectors, which are hard to classify as a whole due to the use of different technologies in one headlamp. An important element are the light sources used in them. Currently, both classic R2 bulbs, halogen bulbs as well as discharge lamps and lenses are in use. Currently, the most popular modern technology in the headlamps is bi-xenon, whose greatest competition is LED technology. Smart lights are also a dynamically developing area.

Research on the impact of the technical condition of vehicle lighting

The study aimed to verify the technical condition of the lighting of vehicles in Greater Poland. For this purpose, 20 randomly selected vehicles were tested at a vehicle inspection station. This study consisted of two parts. First, the operation of the lighting in the tested means of transport was organoleptically checked. For this purpose, the following were checked: operation of the headlights, including an assessment of the condition of bulbs and glass of headlights, stop lights, which should shine much more clearly than the rear position lights. In the next part of the test, the direction indicators are checked. Both the front, side and rear directional lamps should be synchronised. The frequency of the lights should be between sixty and one hundred and twenty flashes per minute. One flash must not be longer than one second. The next stage of the test is to check the operation of other vehicle lamps, such as position, front and rear fog lamps, reversing lamp, emergency lamp. These lights should light up and the lampshades in which they are placed should not have any cracks or be dirty. It should also be checked whether the indicator lamps corresponding to each type of light work and inform the driver about their activation.

The correct operation of the headlights in vehicles is defined in two ways. The first of them is to properly set the tested reflector to obtain the appropriate limit of light and shadow and obtain the appropriate glare effect. The next stage of the study is to determine the physical quantities that characterize the reflector. These include light and luminous intensity. They have a significant impact on the driving comfort of both the driver driving the vehicle and the drivers in the vehicles passed on the road. Lights with inadequate parameters can dazzle the driver coming from the opposite direction or insufficiently illuminate the road. In both cases, there is a risk of an accident. The test was carried out following the guidelines that are used during the technical inspection of the vehicle at the vehicle inspection station.

At the vehicle inspection station, the first measured quantity is the intensity of light, which determines whether the light emitted by the headlamps in the tested vehicle can dazzle drivers driving in the opposite direction to the tested

vehicle (Fig. 2). The device's knob is set in the upper position and the photoresistor is in the leftmost position, which simulates the view of the driver's eyes driving in the opposite direction. The value read from the display is considered to meet the requirements if it does not exceed 1 lux.

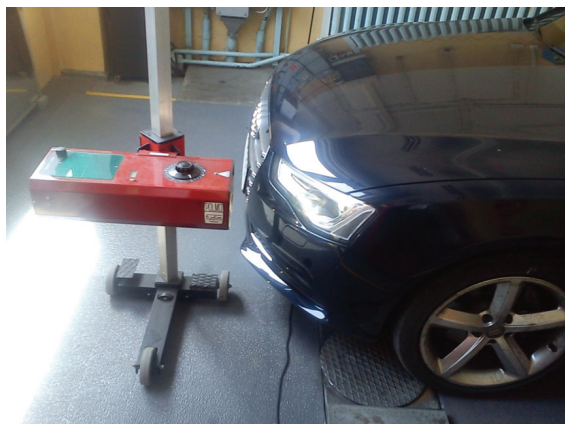


Fig. 2. Inspection of the technical condition of lighting

The next stage of diagnostics is the measurement of the luminous intensity of traffic lights. For this purpose, the highest value of the light indicated by the photoresistor is selected regardless of its position. The luminous intensity of a single driving beam shall be greater than 30 kcd. At the same time, the sum of the luminous intensity of all traffic lights shall not exceed 225 kcd.

The direct light differences between the values of the right and left luminous lights, which regulate the act, also determine the efficiency of traffic lights. If the higher light exceeds 40 kcd, the difference in its value may not be greater than 30%. If the greater light does not exceed 40 kcd, the difference in its value may not be greater than 50%.

To verify the above data, 20 vehicles in Greater Poland were examined. The vehicles were previously unloaded and the tire pressure was adjusted as per the requirements. The initial inspection of the tested vehicles was then started and the results are presented in the table below (GOLEBIOWSKI, STANISŁAWSKI 1998, TRZECIAK 2010).

The test of the headlight settings in vehicles was made using the USP 20 PS device (Fig. 3). Before checking the



Fig. 3. Device type USP-20 PS

Table 2

Results of the initial inspection of the tested vehicles at the vehicle inspection station

Ordinal number	Make of the car	Year of production	Operation of full beam	Operation of dipped beam	Condition of the headlamps	Stop lights operation	Operation of direction indicators	Operation of the front position lamps	Operation of the rear position lamps	Operation of reversing light
1	VW Golf II	1989	works	works	good	works	correct	works	works	works
2	Opel Astra I	1992	works	works	good	works	correct	works	works	works
3	Opel Astra I	1994	works	works	good	works	correct	works	works	works
4	VW Passat B4	1994	works	works	good	works	correct	works	works	works
5	VW Golf III	1995	works	works	good	works	correct	works	works	works
6	Fiat Punto I	1995	works	works	good	works	correct	works	works	works
7	VW Golf III	1996	works	works	good	works	correct	works	works	works
8	Fiat Seicento	1999	works	works	good	works	correct	works	works	works
9	Opel Astra II	1999	works	works	good	works	correct	works	works	works
10	VW Passat B5	2001	works	works	good	works	correct	works	works	works
11	Renault Laguna II	2001	works	works	good	works	correct	works	works	works
12	Audi A4 B6	2003	works	works	good	works	correct	works	works	works
13	Ford Mondeo Mk3	2003	works	works	good	works	correct	works	works	works
14	Renault Clio III	2005	works	works	good	works	correct	works	works	works
15	Peugeot 206	2005	works	works	good	works	correct	works	works	works
16	Opel Zafira B	2005	works	works	good	works	correct	works	works	works
17	Ford Fiesta Mk6	2007	works	works	good	works	correct	works	works	works
18	Renault Laguna III	2008	works	works	good	works	correct	works	works	works
19	Audi A5	2010	works	works	good	works	correct	works	works	works
20	VW Passat B7	2011	works	works	good	works	correct	works	works	works

intensity and brightness of the vehicle lights, each reflector was appropriately set following the legal provisions regarding the limits of light and shadow.

The first of the tests was to determine the intensity of the light of the dipped beam expressed in lux. In the next step, the analysis of the luminous intensity of the road lights was started. The unit for determining the light is a candela. The obtained results are presented in the Table 3.

Table 3

The results of the test of intensity and luminous intensity of dipped beam

Ordinal number	Make of the car	Luminous intensity of the left headlamp [lx]	Luminous intensity of the right headlamp [lx]	Light of the left light [kcd]	Light of the right light [kcd]	The sum of the luminous intensity of the left and right lights [kcd]
1	VW Golf II	0.32	0.32	15	10	25
2	Opel Astra I	0.45	0.36	36	42	78
3	Opel Astra I	0.38	0.41	24	19	43
4	VW Passat B4	0.52	0.47	38	43	81
5	VW Golf III	0.41	0.45	21	27	48
6	Fiat Punto I	0.40	0.42	36	38	74
7	VW Golf III	0.46	0.48	28	29	57
8	Fiat Seicento	0.39	0.43	35	29	64
9	Opel Astra II	0.49	0.49	43	40	83
10	VW Passat B5	0.58	0.54	49	55	104
11	Renault Laguna II	0.54	0.52	67	58	125
12	Audi A4 B6	0.55	0.56	53	49	102
13	Ford Mondeo Mk3	0.42	0.47	56	51	107
14	Renault Clio III	0.53	0.52	53	54	107
15	Peugeot 206	0.57	0.48	52	59	111
16	Opel Zafira B	0.72	0.68	108	120	228
17	Ford Fiesta Mk6	0.28	0.35	47	51	98
18	Renault Laguna III	0.76	0.74	97	104	201
19	Audi A5	0.65	0.66	112	110	222
20	VW Passat B7	0.59	0.62	107	101	208

After analysing the results of the preliminary inspection of vehicle lighting, it can be concluded that all tested vehicles have operational lighting. This is confirmed by the fact that lighting has an impact on road accidents. Each driver can perform such an inspection organoleptically and its results are satisfactory. Upon preliminary evaluation, it appears that the front position, rear position,

reversing, stop and directional lamps function as required. The condition of the tested headlamps is also good or, in some cases, very good (no major scratches and cracks in the glass, permanent fixings in good condition). High beam and dipped beam were analysed separately.

According to the requirements, the maximum value of the dipped beam intensity is 1 lux. After testing randomly selected twenty vehicles, the results are shown in Figure 4.

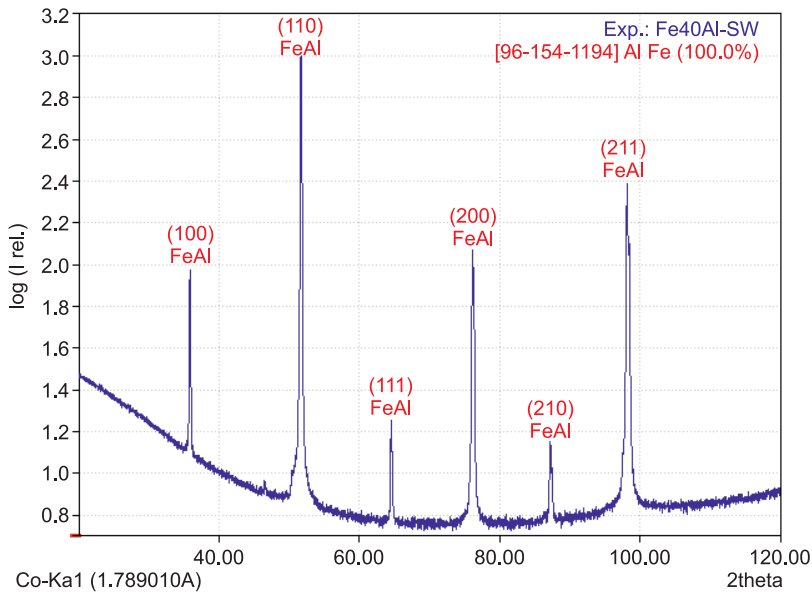


Fig. 4. Luminous intensity of the left and right reflectors [lx]

It was found that all vehicles meet the requirement for the intensity of the luminous intensity of both the right and left reflectors.

The next parameter examined was the luminous intensity of the dipped beam. Pursuant to Polish law, the reflector must shine with a luminous intensity of at least 30 kcd, and the sum of all luminous intensity of the lights must not exceed 225 kcd.

It was found that not all vehicles meet the requirements for traffic lights. In the case of a minimum value of light in four vehicles, it was not reached by the left headlamps, and in five vehicles it was satisfactory. This applies mainly to vehicles manufactured in the early 1990s and earlier, and those in which older technologies were used, both light sources and its radius. In the case of the VW Golf II, the sum of the luminous intensity of all high-beam headlamps did not exceed even 30 kcd, which is why it is recommended to replace the headlamps in this vehicle. In the tested vehicles it was found to be good or very good.

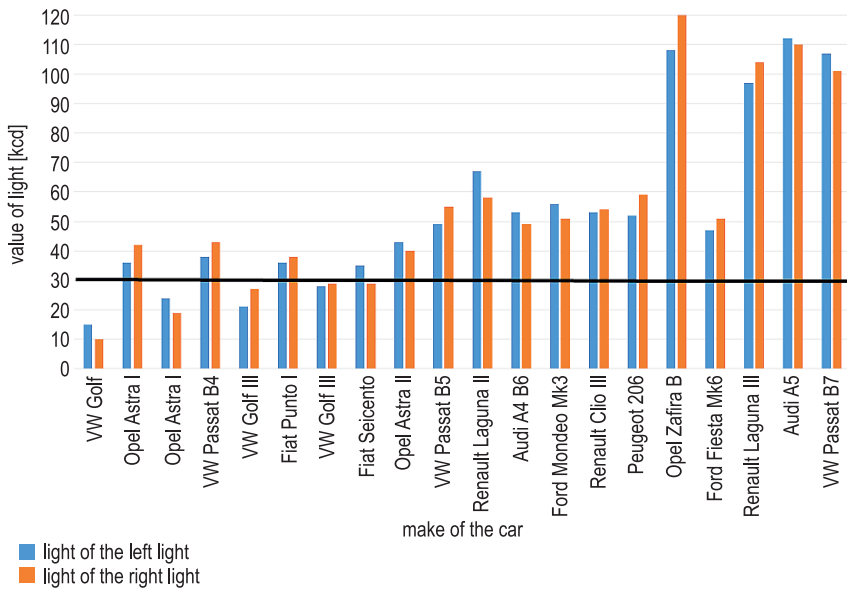


Fig. 5. Light of left and right light

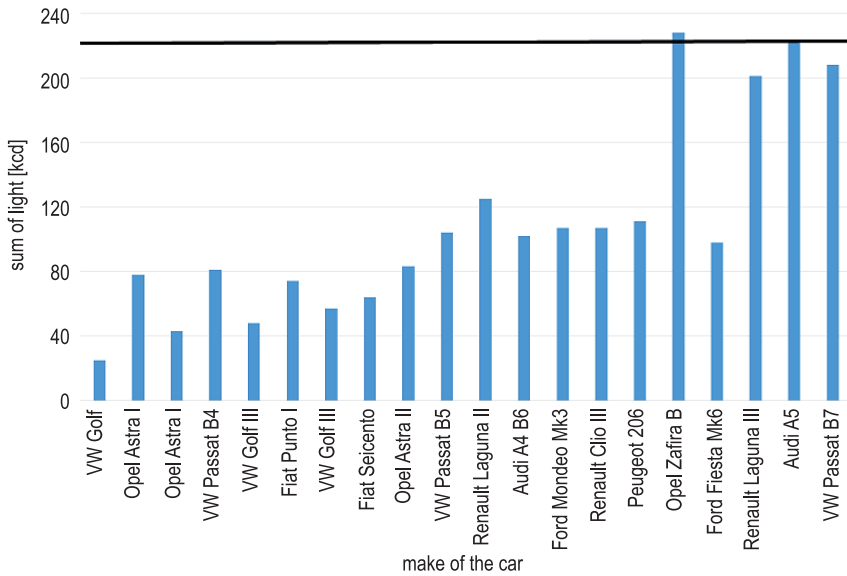


Fig. 6. Total light of lights

The use of new technologies improves visibility on roads, which is especially important in the hours between sunset and dawn. In the diagnostics of vehicles, the importance of examining the technical condition of their lighting is becoming increasingly important, which is why newer and more technologically advanced devices for its testing are being created.

From the research carried out, as well as the statistical data received from the police service, it is clear that most drivers care about the technical condition of the lighting in their vehicles. However, there are significant differences in vehicles in which different technologies are used. The best results of tests are characterised by modern cars equipped with headlamps with discharge lamps.

Characteristics of tires

Tires are another major vehicle component affecting road safety. For this purpose, the tires were tested on public transport buses in Piła, as well as in driving training trucks.

Tires are one of the most important parts of a bus and form part of the vehicle's wheel. One of the elements of the tire is the tread, i.e. the outer part in contact with the road. Depending on what the tire is to be used for and under what conditions it will be used, manufacturers choose the appropriate ridge, shape and hardness of the rubber. The tread pattern is the shape of the grooves, which are designed to drain water so that there is no aquaplaning, i.e. the formation of a thin layer of water between the tire's contact point and the surface on which it rolls. With excessively worn tires, this phenomenon is very common as the tread depth does not allow water to drain away, which results in skidding.

The next element of the tire is the carcass or the bearing part of the tire. It is made of cord, which is connected to the foot. It forms the skeleton of the tire. It is made of several layers of threads arranged at different angles, depending on the type of tire and manufacturer (GORZELANCZYK 2017).

Characteristics of the enterprise MZK PIŁA

The history of Piła urban transport dates back to the 1920s when the first three lines operated. During World War II, the city was so damaged that it was not reopened until July 1, 1957. By the decision of the Provincial National Council in Poznań, the Municipal Transport Plant was established at the Municipal Enterprise of Economy in Piła. Initially, it was located at 10 Kujawska Street. Currently, it is located at 4 Łączna Street (MZK Piła sp. z o.o. 2018).

On December 29, 2000, Miejski Zakład Komunikacji Limited Liability Company in Piła was officially formed as a result of the transformation. At that time, apart from the old rolling stock, the company already had 2 new Neoplan N4009 buses and 8 Neoplan N4016 buses.

There are currently 24 bus lines in Piła. Below is a diagram of the routes. At designated times and seasons they are shortened or extended based on several years of research.

The public transport operator in the analysed city is the Municipal Department of Transport in Piła (MZK). MZK has 47 buses, most of which are low-loader to improve comfort. The brands of used buses include: Jelcz, Neoplan, Solaris and Mercedes (MZK Piła sp. z o.o. 2018).

Tire testing on public transport buses

Tire testing was carried out by measuring the tread height in bus tires in MZK, using an analogue calliper with a depth gauge (PACZYNSKI 2003). This method ensures that correct measurements are made at the level of workshop accuracy. The analogue calliper used for measurements has a measurement accuracy of up to 0.05 mm.

Tread measurements were made in the middle of the tread width. These measurements were made three times for each tire with a 120° shift, which is schematically shown in Figure 7. This allowed measurements to be made at various locations around the circumference of the tires. In this way, it is possible to determine whether the tire has the required tread height or no local wear or wear that disqualifies it from continuing use.

Measurements were made starting from the tire on the driver's side. The next measurements were made in a clockwise direction. The unified measurement process has helped to avoid unnecessary errors in the recording and affiliation of measurement from one particular tire to another (Fig. 8).

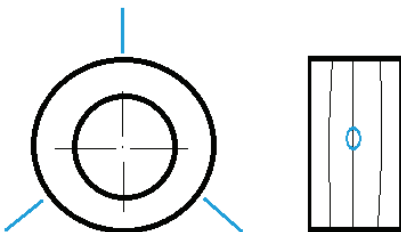


Fig. 7. Places where tread height measurements are made: blue lines characterize the place of measurement at 120°

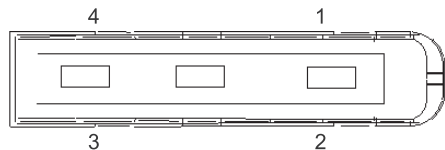


Fig. 8. The order of measurements

Every time the tread height was measured on the bus, the meter reading was recorded along with the date of measurement. This allowed the kilometres travelled and tread wear in the analysed period to be analysed.

The tests covered a four-month period of bus operation in urban traffic conditions. The first measurement was made to determine the output data. The second measurement of the tire tread on MZK buses was made after two months, and the third (last) measurement was made after the fourth month from the beginning of the measurements. The research was carried out on 16 randomly selected buses that are equipped with MZK. The list of selected buses is presented in Table 4.

Table 5 and Figure 9 summarize the average tread height of the first, second, third and fourth wheel after the last measurement. The minimum permitted tread height on the buses in question should be 1.6 mm.

Table 4

List of selected MZK Pila buses for tire wear tests

Bus brand	Bus model	The number selected for testing	Quantity on stock MZK Pila	Bus length [m]
Solaris	Urbino 10	2	4	10
Neoplan	N4411	2	6	10
Neoplan	N4016	4	7	12
Jelcz	120M	2	3	12
Mercedes-Benz	Citaro	3	7	12
Solaris	Urbino 12	3	20	12

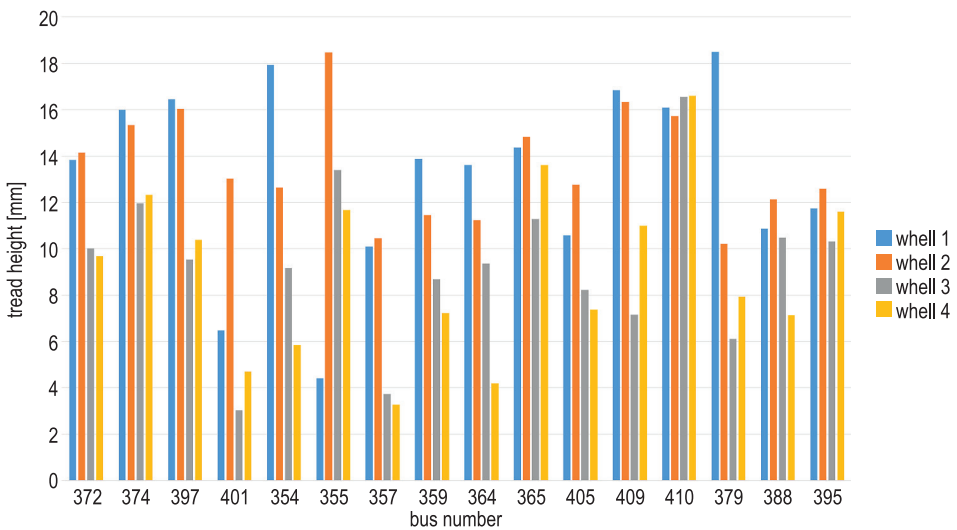


Fig. 9. Bus tread height MZK Pila

Table 5

Tread height in buses MZK Pila

Side number	The average tread height of the first wheel [mm]	The average tread height of the second wheel [mm]	Average tread height of third wheels [mm]	The average tread height of the fourth wheels [mm]
372	13.82	14.15	10.02	9.67
374	16.00	15.33	11.97	12.33
397	16.45	16.05	9.53	10.38
401	6.47	13.03	3.02	4.70
354	17.93	12.65	9.17	5.85
355	4.40	18.47	13.40	11.68
357	10.10	10.45	3.73	3.27
359	13.88	11.45	8.68	7.22
364	13.60	11.23	9.37	4.20
365	14.37	14.82	11.27	13.62
405	10.58	12.75	8.22	7.37
409	16.83	16.33	7.15	11.00
410	16.10	15.73	16.55	16.61
379	18.50	10.20	6.10	7.92
388	10.87	12.13	10.48	7.12
395	11.73	12.58	10.32	11.60
Arithmetic average	13.23	13.58	9.31	9.03

The number of kilometres travelled by buses is presented, compared to the average of all buses. Two Jelcz 120M buses (side numbers 364 and 365) whose drivers enjoyed a holiday break were removed from the list. The tests were conducted for six months of use. The presented data reflect, in a real way, a comparison of buses that are operated in a continuous manner without interruption. The table also shows the sum of kilometres travelled.

Due to the preservation of the actual image data for tire tread wear, buses that had tires replaced in a given wheel or wheels 3, 4 (due to the twin wheels) were excluded from the calculations (Tab. 7 and Fig. 9). These exclusions include buses and selected wheels with side numbers:

- Wheel 1: 364, 365, 379.
- Wheel 2: 364, 365, 355.
- Wheels 3: 364, 365, 372, 374, 388.
- Wheels 4: 364, 365, 372, 374.

Table 6

Bus mileage summary MZK Piła

Number	Side number	Number of kilometres after 1 measurement [km]	Number of kilometres after the 2 nd measurement [km]	Sum kilometres [km]
1	372	8,882	7,910	16,792
2	374	7,289	8,401	15,690
3	397	8,408	1,816	10,224
4	401	8,630	9,198	17,828
5	354	6,988	5,460	12,448
6	355	7,677	6,875	14,552
7	357	11,308	6,925	18,233
8	359	8,403	3,174	11,577
9	405	11,996	11,742	23,738
10	409	13,654	15,326	28,980
11	410	8,659	8,007	16,666
12	379	12,339	13,895	26,234
13	388	12,400	14,027	26,427
14	395	11,224	13,234	24,458
Sum		137,857	125,990	263,847
Arithmetic average		9,847	8,999	18,846

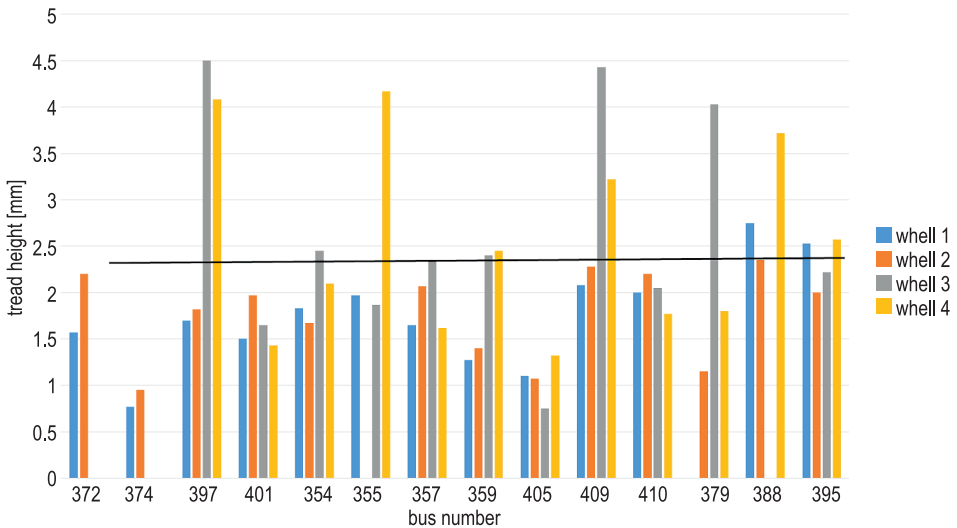


Fig. 10. Consumption of bus tires: minimum permissible tread depth

Table 7

Tread wear for bus tires

Number	Side number	The sum of wear – the front left wheel [mm]	Total tire wear – front right wheel [mm]	Sum of tire wear – rear right wheels [mm]	Sum of tire wear – rear left wheels [mm]
1	372	1.57	2.2	exchange	exchange
2	374	0.77	0.95	exchange	exchange
3	397	1.7	1.82	4.5	4.08
4	401	1.5	1.97	1.65	1.43
5	354	1.83	1.67	2.45	2.1
6	355	1.97	exchange	1.87	4.17
7	357	1.65	2.07	2.35	1.62
8	359	1.27	1.4	2.4	2.45
9	364	exchange	exchange	exchange	exchange
10	365	exchange	exchange	exchange	exchange
11	405	1.1	1.07	0.75	1.32
12	409	2.08	2.28	4.43	3.22
13	410	2	2.2	2.05	1.77
14	379	exchange	1.15	4.03	1.8
15	388	2.75	2.35	exchange	3.72
16	395	2.53	2	2.22	2.57
	Sum	22.72	23.13	28.70	30.25
	Arithmetic average	1.75	1.78	2.61	2.52

There was a six-month gap between the first and the third measurement. The problem when planning the tests was the possibility of replacing the tires on the bus in which the tread height was tested. For the research to make sense, a larger number of buses were adopted at the beginning. In total, 16 buses from MZK were selected for testing. Two of them were excluded for the period of school holidays, while in five during the tests, one or two tires and sometimes four tires were replaced.

The research shows that the tires at the back of the buses wear one and a half times faster than the tires on the axles at the front of the vehicle. This is mainly due to frequent braking and acceleration, turning of the wheels during manoeuvring, bruising the sides with curbs and the implementation of courses with fully filled buses contributes to the intensification of tire wear. In addition, brushing against curbs causes a negative impact on the tire structure and shortens the service life, despite sufficient tread height.

Tests of tires in the truck

The subject of the research were tires mounted on two MAN trucks with trailers used by one of the driving schools in Piła. Below is the scope of the research carried out. Possible tire damage includes uneven or excessive tire wear or mechanical damage to the tires.

The measurement of tires includes an assessment of the technical condition of the tires (the nature of tread wear, depth of tread pattern, number, dimensions and the distribution of damage on the circumference of the tire).

When inspecting the wheels, special attention was paid to:

- compliance of used rims and tires with the requirements of the manufacturer of the given vehicle,
- tread depth,
- the nature of tread pattern wear,
- assessment of noise emission from the work of tires,
- checking the arrangement of tires and rims after assembly,
- checking for damage or deformation of rims,
- checking for the presence of foreign bodies in the tires,
- checking for mechanical damage (bulges, cracks, tire defects).

Tests on the condition of truck tires used for driving lessons consisted of measuring twenty-four tires at regular intervals, at the same points using an electronic calliper. The MAN TGL 12.240 + Trailer and MAN FH2000 + Trailer were used for the tests.



Fig. 11. MAN TGL 12.240 + trailer

MAN year of production 2009 – a vehicle used only for driving lessons. Trailer year of production 1996 – also used only for driving lessons. Both the car and the trailer were used unladen.

The first is: MAN year of production 2009. The vehicle was used only for driving lessons. This set also included a trailer from 1996 used only for driving lessons.



Fig. 12. MAN FH2000 + trailer

The tire tread height test was carried out at three points on the tire width, in the inner, middle and outer parts of the vehicle. The tests took place after every 40 hours of work of a given research object.



Fig. 13. Places of measurements

Figures 14-17 show the measurement results (mm) of the tread depth of individual tires. There were a total of 30 measurements, once a week, from August 30, 2014 to February 1, 2015 (it was each Sunday after the end of work). The starting point of the charts was set at 1.6 mm as the minimum tread height allowed for traffic. The exception is the chart showing the tread height of the MAN FH2000 trailer tires, due to the low tread height.

The research shows that in trucks used for driving lessons, tire wear is not uniform over their entire width. Tires wear out as follows:

1. With the front axles, the tires wear out in the shape of a trapezium – internal and external parts more than the middle. The effect on this way of wear is probably due to driving on the manoeuvring square, where the maximum turns are performed at a standstill almost every time during parking manoeuvres.
2. With the rear axles, the outer part of the right-hand outer tire is the most worn. This kind of wear is also caused by driving on the manoeuvring square (e.g. driving on a curve).

3. For trailers, almost 75% of the course is spent on the manoeuvring square where one of the most difficult tasks is driving in a lane forward and backward in an arc that requires turning to the right. Trainees practicing this manoeuvre mainly use the tire located on the front axle on the right outer side.

4. Additionally, the surface of the manoeuvring square used by the studied driving school is concrete, which wears tires much more than asphalt.

5. It is advisable to replace the front right tires, both inside and outside, with the MAN FH2000 car trailer, due to the tread height being too low. It was done immediately after the measurements.

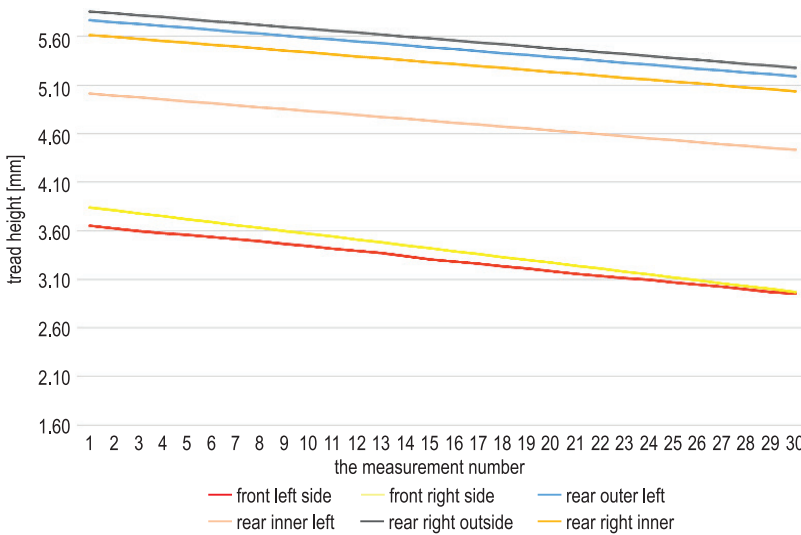


Fig. 14. Tire tread height MAN TGL 12.240

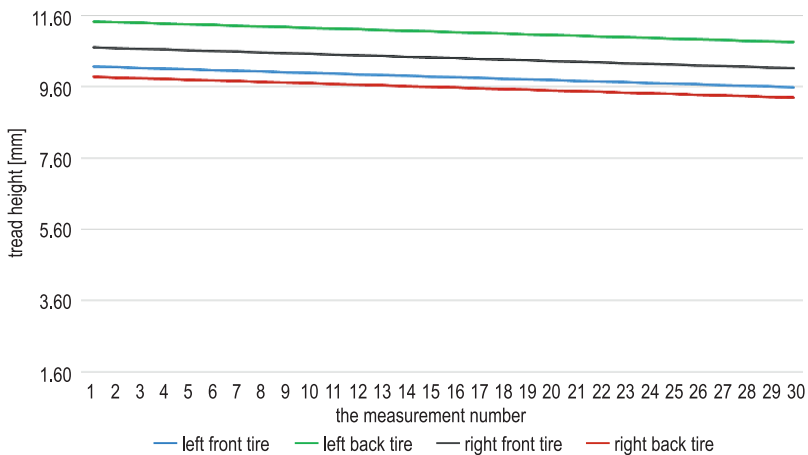


Fig. 15. Tire tread height of the car trailer MAN TGL 12.240

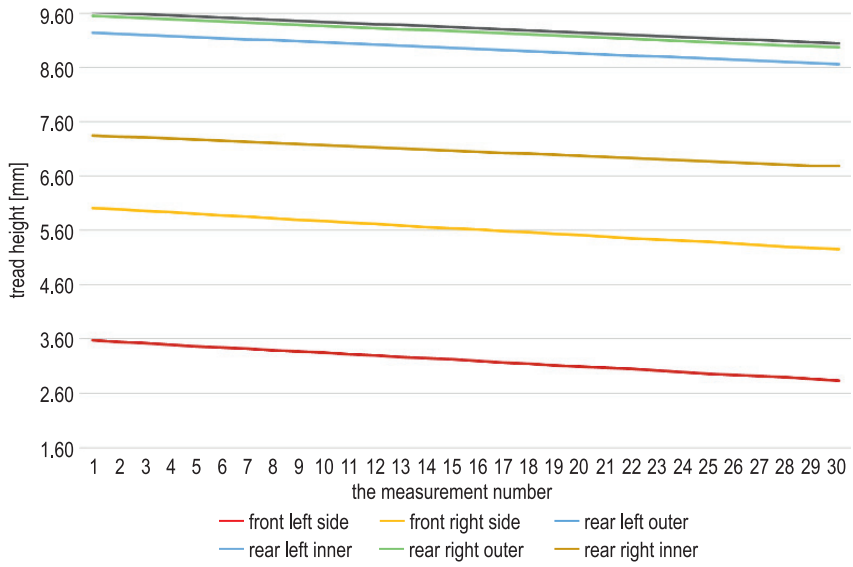


Fig. 16. Tire tread height MAN FH2000

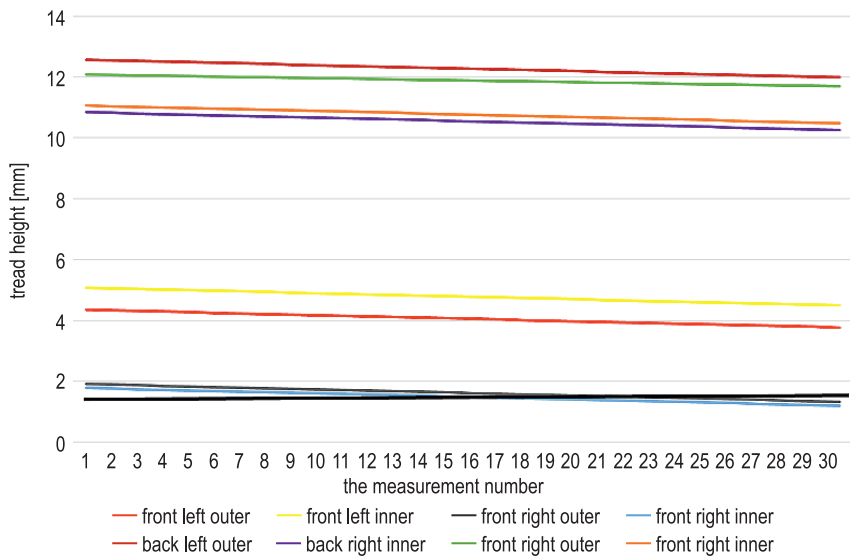


Fig. 17. Tire tread height of the car trailer MAN FH2000

Conclusion

Based on the tests, as well as the statistical data received from the Police Headquarters, it is clear that most drivers care about the technical condition of lighting in their vehicles and the truck tires used for learning to drive and buses are in good condition and this should not affect the safety of vehicles on the roads in Greater Poland and Poland.

The tested vehicles can travel on roads without affecting safety. However, according to police statistics, there are accidents resulting from deficiencies in lighting or disability every year. Although these are only a small fraction of the total number of accidents, however, with an appropriate diagnostic approach and subsequent repair of damaged components, these events could be avoided.

Author Contributions: PG: Preparation of the entire article

Compliance with ethical standards

Conflict of interest: The authors declare that they have no conflict of interest.

References

- AMBROŻUK D., WESOŁOWSKI K. 2017. *Technical condition of means of transport as the cause of transport damage*. Scientific Journals of the University of Szczecin Problems of Transport and Logistics, 39: 161-172.
- GOŁĘBIEWSKI S., STANISŁAWSKI I. 1998. *Car control tests*. WKiŁ, Warszawa.
- GORZELANCZYK P. 2017. *The research of tread wear process on the basis of bus's tyres used by PT operator in Pila*. Coaches. Technology, Operation, Transport Systems, 12.
- KULAKOWSKA A., PATYK R. 2013. *Analysis of the impact of the technical condition of vehicles on the occurrence of road accidents*. Autobusy. Technika. Eksploatacja. Systemy Transportowe, 14(10): 170-175.
- MZK Piła sp z o.o. 2018. www.mzk.pila.pl (access: 1.12.2018).
- PACZYNSKI P. 2003. *Technical metrology. A guide to lectures, exercises and laboratories*. Publisher of Poznan University of Technology, Poznań.
- Polish Police. 2018. <http://www.statystyka.policja.pl> (access: 1.12.2018).
- TRZECIAK K. 2010. *Diagnostics of passenger cars*. WKiŁ, Warszawa.
- Ustawa z 16 grudnia 2010 r. o publicznym transporcie zbiorowym. Dz.U. of 2011 No. 5 item 13, <http://prawo.sejm.gov.pl/isap.nsf/DocDetails.xsp?id=WDU20110050013> (access: 1.12.2018).



INFLUENCE OF PLASTIC DEFORMATION ON THE ELECTROCHEMICAL PROPERTIES OF X5CRNI18-10 STEEL

Wojciech Rejmer

ORCID: 0000-0002-1955-1553

Faculty of Technical Sciences

University of Warmia and Mazury in Olsztyn

Received 4 November 2020, accepted 9 December 2020, available online 9 December 2020.

Key words: corrosion, electrochemistry, stainless steel, impedance spectroscopy, Tafel plots.

Abstract

The purpose of this study was to determine the effect of plastic deformation on the electrochemical properties of X5CrNi18-10 steel. The tested material belongs to the group of stainless steels with low carbon content, and it is used in many industries due to its high corrosion resistance. In most applications of the tested material, it is formed into complicated shapes and exposed to aggressive environments. Examples include the applications in medicine (implants) as well as in civil engineering and nuclear power plants. Different effects of deformation on anti-corrosion properties have been described in the literature. Samples with 5 different deformations were obtained in the present experiment. Electrochemical direct electrical current and alternating electrical current tests were performed for the obtained materials. The tests were carried out in a 1 molar sodium chloride solution. The study revealed an increase in the corrosion resistance of samples with increasing strain in the tested strain ranges.

Introduction

Steel 1.4301 belongs to the group of corrosion-resistant steels (EN 10088-1:2014), and it has a wide range of applications. In the automotive industry, it is used, among others, as a construction material for the production of exhaust systems, catalyst and turbocharger housings, fuel tanks, truck and bus chassis, external and internal decorative elements, suspension elements, safety cages and road tankers. Various types of stainless steel are widely used due to their corrosion resistance and the possibility of producing complex and visually attractive shapes (KULAKOWSKI, ROKOSZ 2017). Stainless steel is also used in the production of cookware. It is estimated that around 43% of kitchen utensils are made of stainless steel (BERNSTEIN 1977, SANTONEN et al. 2010). Most of the stainless steel used in cookware contains approximately 18% chromium, which ensures optimal corrosion resistance. Apart from chromium, it also contains nickel in the amount of 8-10% (BASSIONI et al. 2015). Stainless steel is also widely used in construction. The most popular applications include the construction of glazed roofs and facades, as well as elevators and escalators. It is used for the construction of barriers and balustrades (WCIŚLIK 2017). Austenitic stainless steels are also used in medicine. They are often used in the production of orthopedic implants due to their properties, including the resistance to corrosion and fatigue, as well as high resistance to fracture. These properties are important in the selection and modification of materials for biomedical applications (RYAN et al. 2006, ALVAREZ et al. 2008). Nuclear power generation is yet another branch of industry where stainless steels are used. The construction materials for nuclear power plants should preserve the integrity of fuel rods and prevent the release of radioactive materials from the fuel into the coolant. The materials are also exposed to aggressive environments. The aggressiveness of the environment is caused by the velocity of a neutron flux combined with a high temperature. Neutron radiation causes the displacement of atoms in the nodes of a crystal lattice (*Stress Corrosion Cracking...* 2011). The above leads to void swelling, phase instability and creep that increases with the intensity of neutron radiation. To meet these conditions, the chemical composition/microstructure of stainless steels must be changed, for example by introducing smaller amounts of alloying elements such as Ti, Si and P. Recent research into the use of stainless steels as lining for nuclear fuel rods and fuel assembly components has shown that yttrium and oxide precipitates act as stable obstacles to the movement of atoms, and help block radiation. Stainless steels have also been used as a replacement for copper alloys in tube bundles for feedwater heaters. Products made from copper alloys cause galvanic corrosion, thus disturbing heat transfer (VENKATRAMAN 2013). Austenitic steels are characterized by high corrosion resistance in acidic environments, which, however, changes in response to plastic deformation. Samples deformed by cold rolling have lower corrosion resistance than non-deformed samples. Corrosion

resistance changes in environments rich in chloride ions, which cause pitting corrosion (FREIREA et al. 2011). It can be concluded that plastic deformation produced in a cold environment and at high speeds leads to the formation of local micro-cells (RUTKOWSKA-GORCZYCA et al. 2009). An increase in corrosion resistance was observed when crushing samples of AISI 321 steel to the level of 0.86. The steel used in the study had a crystallographic system of regular face-centered unit cells. Additionally, samples of different morphology were obtained by heat treatment. A decrease in corrosion resistance resulting from deformation was observed only in samples with the smallest grain sizes. Deformed samples with larger grain sizes were characterized by higher corrosion resistance. It appears that this effect is caused by the development of austenite crystallographic planes, which reduces the influence of martensitic phase formation (TIAMIYU 2019). In the tests that revealed an increase in corrosion potential, the applied deformations were single-folded, and the tests were carried out at a constant strain rate. A decrease in corrosion potential was observed for small plastic deformations in the compression cycles, leading to an increase in the hardness of stainless steel. In addition, several rolling cycles (strains greater than 0.2) were required to achieve higher levels of deformation in the rolling process. The electrochemical parameters of the analyzed samples may be influenced by the extent of deformation and the related changes in the material's structure. A breaking test was performed to examine the electrochemical and structural parameters of AISI 304 steel within the ranges of elastic and plastic strains. Comprehensive research, including electrochemical and structural tests, demonstrated that the type of deformation exerted varied effects on the electrochemical parameters of the tested material. According to research, elastic deformations do not affect the material's susceptibility to corrosion. Plastic deformations caused a significant decrease in corrosion potential. The tests were carried out during stretching. The decrease in corrosion potential during deformation was attributed to the formation of cracks in the passive oxide layer. The distortion of the layer structure probably resulted in the formation of new active surfaces enabling faster electrochemical processes to take place (NAZAROV et al. 2019). The aim of the present study was to determine the influence of plastic deformation in the tensile cycle on the electrochemical properties of X5CrNi18-10 steel (1.4301 or AISI 304). The tests were carried out 48 h after grinding the sample in order to enable the formation of an oxide layer.

Materials and Methods

Samples of X5CrNi18-10 steel used in the experiment are presented in Figure 1. The samples were cut out from a 5 mm thick metal sheet with the use of the ZAP BP09d electro-erosive cutter.

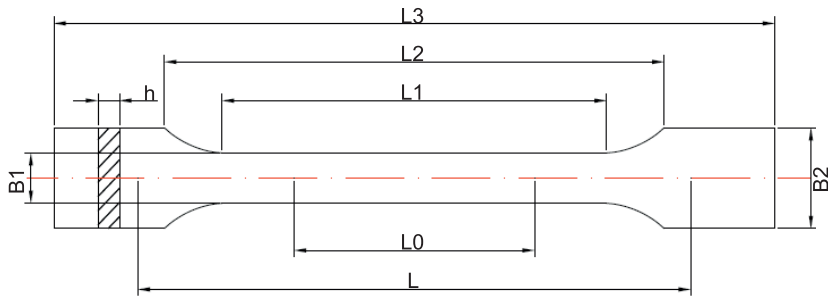


Fig. 1. Sample shapes (description in the text)

The dimensions of the samples were as follows: $L_0 = 30$ mm, $L_1 = 45$ mm, $L_2 = 60$ mm, $L_3 = 125$ mm, $b_1 = 5$ mm, $b_2 = 10$ mm, $h = 5$ mm. The tensile tests were performed in accordance with Standard PN-EN ISO 6892-1. The samples were stretched at a speed of 2.5 mm/min on the Tira Test 27100 testing machine. The following deformations were obtained: 0.07; 0.12; 0.16; 0.20; 0.23. Three samples were prepared for each level of deformation. In addition, three samples were left undistorted. The samples were ground on a laboratory grinder with the use of sandpaper graded from 200 to 800 to the resulting roughness R_a of 0.4 to 0.5 μm . The test samples were left in the desiccator for 48 h and then their roughness was measured again. The samples were cleansed with acetone and placed in an electrochemical vessel (Fig. 2). The necking of the samples was the place isolated within the electrochemical unit with the use of a 5 mm diameter o-ring. Therefore, electrochemical data were obtained for the area of 19.6 mm².

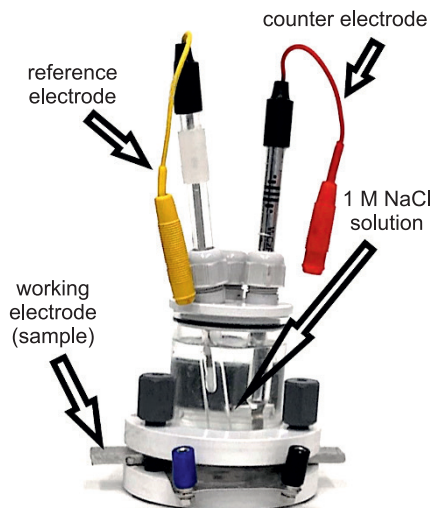


Fig. 2 . Electrochemical vessel

A 1 M NaCl solution was poured into the electrochemical vessel with the sample attached, which allows for linear changes in the conductivity of the solution without the involvement of processes related to changes in the ion activity coefficient. A silver chloride electrode as the reference electrode and a platinum electrode as the counter electrode were placed in the vessel. The Lugin capillary was placed on the reference electrode and positioned 0.5 mm above the sample. The electrodes and the sample were connected to an electrochemical unit – ATLAS 1131 EU&IA by Atlas-Solich. The system was then stabilized to steady-state potential for 6 h. The LPR was measured by lowering the potential of the working electrode by 50 mV below the stationary potential, and then increasing the potential to 50 mV above the stationary potential. Changes in the potential occurred at a rate of 1 mV/s. Impedance spectroscopy was carried out using the amplitude of potential changes of 50 mV. The measurements were performed in the frequency range of alternating current of 100 kHz to 1 mHz, using the AtlasCorr program, and the results of the analysis were processed using the AtlasLab program.

Results

The values of corrosion potential and polarization current density were obtained from the Tafel curves. An exemplary plot of the dependence of the sample potential on the logarithm of the absolute value of polarization current density determined for an undistorted sample is shown in Figure 3. Figure 4 shows the dependence of corrosion potential on the extent of plastic deformation.

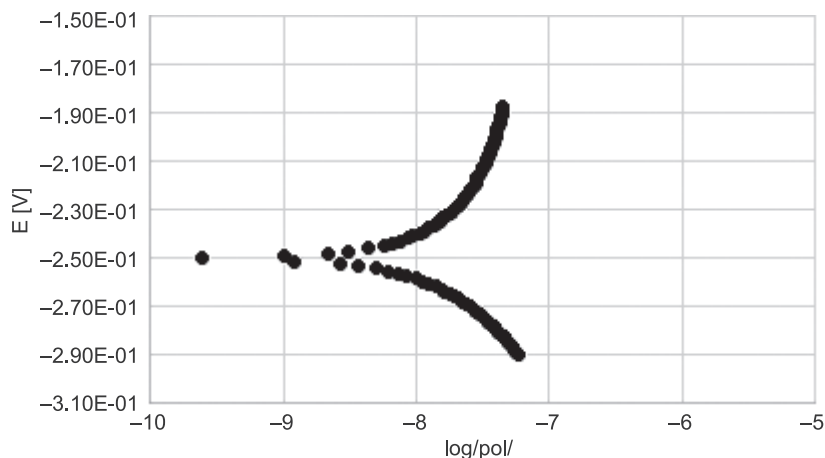


Fig. 3. The dependence of the sample potential on the logarithm of the absolute value of polarization current density determined for an undistorted sample

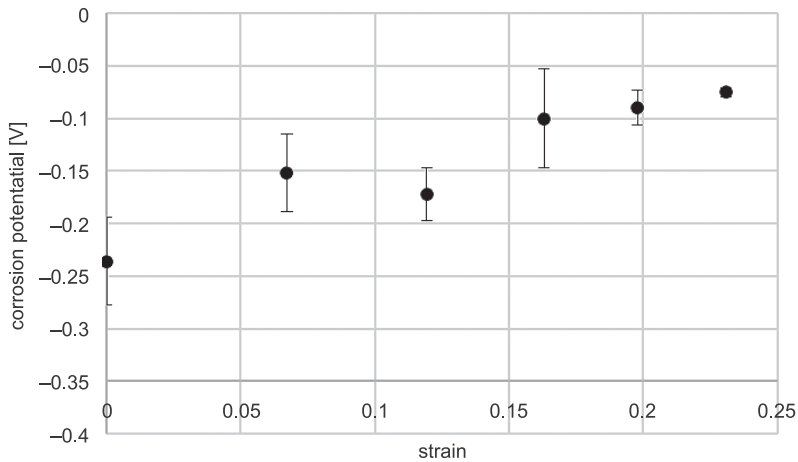


Fig. 4. The dependence of corrosion potential on plastic deformation

In the tested material, the value of corrosion potential measured against the silver chloride electrode increased proportionally to deformation. The measured values ranged from -0.24 to -0.075 V. The values of corrosion potential increased with increasing deformation. The only exception was the sample with a deformation value of 0.12. The remaining samples differed significantly from the non-deformed sample. A comparison of samples with deformation of 0.07 and materials with deformations of 0.2 and 0.23 revealed a significant increase in potential. Corrosion potential is a measure of the energy required for the electrochemical oxidation process to occur. The higher the potential value, the greater the material's resistance. In the analyzed specimens, deformation contributed to an increase in corrosion resistance in the test solution.

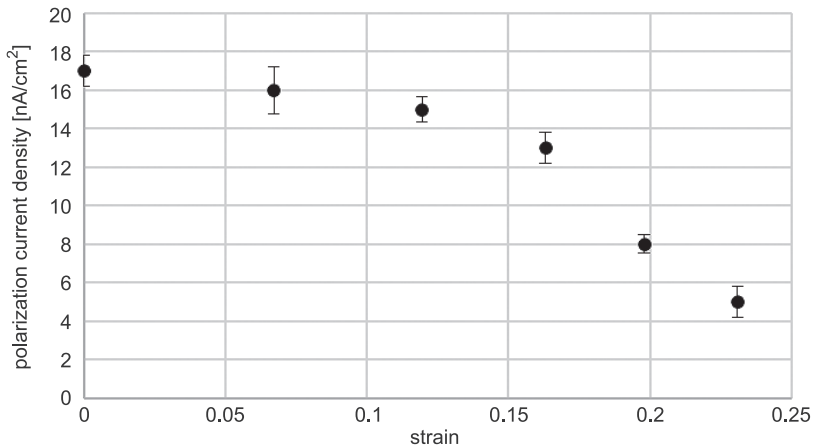


Fig. 5. The dependence of corrosion current density on the plastic deformation of samples

Another parameter determined based on an analysis of Tafel curves was corrosion current density. The values of corrosion current density for materials with specific deformations are shown in Figure 5.

Corrosion current density is inversely proportional to deformation. The highest value of corrosion current density was noted for the non-deformed sample (17 nA/cm²). The lowest value of corrosion current density was observed for the sample with a strain of 0.23. The value of corrosion current density for the most deformed sample was 5 nA/cm². Current density decreased considerably after exceeding the deformation value of 0.16. The measured current densities for strains greater than 0.12 differ significantly from those determined for the undistorted sample. It should be noted that corrosion current densities were low in all cases, and remained within the nanoampere limits. The greater the value of current density, the greater the exchange of electrons on a given surface. In the tested samples, the number of oxidation reactions decreased with increasing strain.

In the next step, deformed samples were tested to determine their behavior in response to alternating current, using the EIS method. The impedance spectra in the form of Nyquist plots are presented in Figure 6.

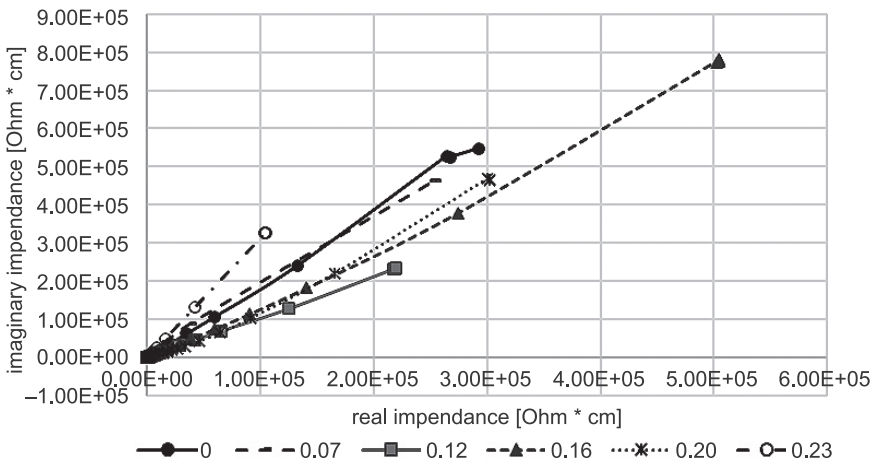
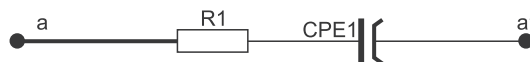


Fig 6. Impedance spectra of deformed samples

The Nyquist plots for all tested samples have the same shape of straight lines, which means that the equivalent circuit that best approximates the tested sample is a series connection of a resistor and a variable phase element (Fig. 7).



The above implies that no new chemical substances appear on the tested surfaces as a result of deformation, which makes it possible to meet the condition of the low invasiveness of the test with regard to the material's structure. It can be concluded that only the quantitative ratio of the substances already present on the material's surface changes in response to deformation. The highest real impedance was determined in samples with a deformation value of 0.16, and the lowest real impedance was noted in the most deformed samples. The second highest corrosion resistance was noted in non-deformed samples and samples with a deformation value of 0.2. The lowest values of real impedance were observed in the most deformed samples. By analyzing the slope of the curve relative to the axis of real impedance, we can assess the extent to which a given surface is covered with a non-conductive layer. In the present case, metal oxides constitute the non-conductive element. The sample that is most similar to an ideal capacitor and thus has the largest amount of metal on the surface is probably the most deformed sample. The slope of the curve in the direction of the X-axis increases with the extent of deformation up to the level of 0.12. The subsequent curves represent Nyquist plots further away from the X-axis. It can be assumed that the percentage of surface covered with oxides decreases with increasing deformation.

Discussion

The deformation of samples made of X5CrNi18-10 steel increases the corrosion resistance of the material within the range of the tested deformations, provided that only DC tests are taken into account. Corrosion potential, which determines the activation energy of the corrosion process, increases. Corrosion current density is reduced, which implies that fewer corrosion processes occur. The impedance spectra show that the tested surface has oxide characteristics rather than metallic characteristics, which affects its electro-insulating properties. In a study by RYBALKA et al. (2006), stainless steel with a chromium content of 12.4% exhibited different impedance spectra with a more metallic character. In the presented research, higher chromium content led to a more oxide character. The morphology of oxide coating may have a greater influence on electrochemical processes taking place during the operation of alternating current. It appears that plastic deformation may favor chromium passivation in the presence of air. Such a mechanism is supported by research conducted by NAZAROV et al. (2019). The above effect may lead to an increase in the amount of oxides, and the observed decrease in corrosion potential and polarization current density. The results of the EIS test may prove the homogeneity of the oxide layer on the steel surface. In the tested samples, the homogeneity of the oxide layer probably

increases to a deformation value of 0.12. After exceeding this level, the amount of oxides continues to increase, but a larger number of discontinuities appear, resulting in greater slopes of the impedance spectrum towards the OY axis (imaginary impedance). This effect may be caused by change in the valence of chromium in oxide layers which may be supported by a shift of potential, a sharper decrease in current density and the slopes of impedance spectra after exceeding a strain of 0.12. In a study by MARIJAN and GOJIC (2002), such an effect was found to be indicative of change in the valence of chromium oxide, but in the present experiment, this effect was caused by forced potential changes. From an electrochemical point of view, an increase in strain can exert a similar effect by decreasing the potential for chromium oxide formation and increasing the thickness of the passive layer, as demonstrated by ZHENG et al. (2018).

References

- ALVAREZ K., SATO K., HYUN S.K., NAKAJIMA H. 2008. *Fabrication and properties of Lotus-type porous nickel-free stainless steel for biomedical applications*. Materials Science and Engineering C, 28: 44-50.
- BASSIONI G., KORIN A., EL-DIN SALAMA A. 2015. *Stainless Steel as a Source of Potential Hazard due to Metal Leaching into Beverages*. International Journal of Electrochemical Science, 10: 3792–3802.
- BERNSTEIN I.M. 1977. *Handbook of stainless steels*. McGraw-Hill, New York.
- EN 10088-1:2014. *Stale odporne na korozję*. Część 1. Wykaz stali odpornych na korozję.
- FREIREIRA L., CARMEZIMA M.J., FERREIRAA M.G.S., MONTEMOR M.F. 2011. *The electrochemical behavior of stainless steel AISI 304 in alkaline solutions with different pH in the presence of chloride*. Electrochimica Acta, 56: 5280–5289.
- KULAKOWSKI M., ROKOSZ K. 2017. *Stopowe stale austenityczne, ferrytyczne i duplex używane w transporcie*. Autobusy, 7-8: 357–362.
- MARIJAN D., GOJIC M. 2002. *Electrochemical study of the chromium electrode behaviour in borate buffer solution*. Journal of Applied Electrochemistry, 32: 1341–1346.
- NAZAROV A., VIVIER V., VUCKO F., THIERRY D. 2019. *Effect of Tensile Stress on the Passivity Breakdown and Repassivation of AISI 304 Stainless Steel: A Scanning Kelvin Probe and Scanning Electrochemical Microscopy Study*. Journal of The Electrochemical Society, 166: C3207-C3219.
- PN-EN ISO 6892-1. *Metale. Próba rozciągania*. Część 1. *Metoda badania w temperaturze pokojowej*.
- RUTKOWSKA-GORCZYCA M., PODREZ-RADZISZEWSKA M., KAJTOCH J. 2009. *Corrosion resistance and microstructure of steel AISI 316L*. Metallurgy and Foundry Engineering, 35: 35–43.
- RYAN G., PANDIT A., APATSIDIS D.P. 2006. *Fabrication methods of porous metals for use in orthopaedic applications*. Biomaterials, 27: 2651-2670.
- RYBALKA K.V., BEKETAeva L.A., DAVYDOV A.D. 2006. *Electrochemical behavior of stainless steel in aerated NaCl solutions by electrochemical impedance and rotating disk electrode methods*. Russian Journal of Electrochemistry, 42: 370–374.
- SANTONEN T., STOCKMANN-JUVALA H., ZITTING A. 2010. *Review on toxicity of stainless steel*. Finnish Institute of Occupational Health, Helsinki.
- Stress Corrosion Cracking in Light Water Reactors: Good Practices and Lessons Learned*. 2011. International Atomic Energy Agency, Vienna.

- TIAMIYU A.A., EDUOK U., SZPUNAR J.A., ODESHI A.G. 2019. *Corrosion behavior of metastable AISI 321 austenitic stainless steel: Investigating the effect of grain size and prior plastic deformation on its degradation pattern in saline media*. Scientific Reports, 9: 1–18.
- VENKATRAMAN M., PAVITRA K., JANA V., KACHWALA T. 2013. *Manufacturing and critical applications of stainless steel – An Overview*. Advanced Materials Research, 794: 163–173.
- WCIŚLIK W., KOSSAKOWSKI P., SOKOŁOWSKI P. 2017. *Stainless steel in building structures – advantages and examples of application*. Structure and Environment, 3: 191–198.
- ZHENG M., SHUAI M., YU J. 2018. *Influence of deformation on electrochemical properties of Q235 steel*. Korozja i ochrona materiałów, 62(3): 108–114.



VIABILITY ANALYSIS OF PINE SAWDUST DRYING IN A FOUNTAIN DRYER

Konrad Rojcewicz¹, Zbigniew Oksiuta²

¹ORCID: 0000-0003-4974-4628

²ORCID: 0000-0002-8719-157X

Faculty of Mechanical Engineering
Białystok University of Technology

Received 12 September 2020, accepted 28 November 2020, available online 3 December 2020.

Keywords: sawdust, fountain dryer, fountain bed, conical spouted bed, pellets, sieving analysis, BET method.

Abstract

This article presents an analysis of the physico-chemical properties of pine sawdust originating from the area of the Knyszyńska Forest, in the context of the possibility of the sawdust drying in a fountain dryer. Several tests were carried out on dry pine sawdust with 45% moisture, including chemical composition, calorific value, ash content as well as morphological changes of wet and dried material. The water storage mechanism in chips and the mechanism of formation of a fountain bed were also discussed. Based on the obtained results, several technical solutions and modifications of the fountain dryer were proposed. These modifications enable sawdust of heterogeneous size and shape to be dried in a fountain dryer as well as additional functional properties.

Nomenclature

- A – is the content of volatiles in the analytical sample [%_{max}]
 m_1 – is the mass of the crucible
 m_2 – is the mass of the crucible with the raw material being burnt
 m_3 – the mass of crucible with ashes
 N – the Avogadro's number

Correspondence: Konrad Rojcewicz, Katedra Inżynierii Materiałowej i Produkcji, Wydział Mechaniczny, Politechnika Białostocka, ul. Wiejska 45C, 15-351 Białystok, e-mail: krojcewicz@gmail.com.

- w_p – the surface occupied by a particle in the surface of the test sample
 α_p – the amount of the gas absorbed
 S_p – specific surface area
 S^i – airflow [dm^3/h]
 t – time [s]
 Y – humidity [%]
 T – temperature [$^{\circ}\text{C}$]
 V – sample volume [ml]

Introduction

Forest and agricultural materials are used for the production of fuel biomass. In the case of biomass from the forest, one can obtain sawdust with different morphology (size and shape), moisture content and physicochemical properties. The problem is also the content of solid impurities and the elemental composition, e.g. the content of chlorine which emits dioxins which are hazardous to health during combustion. The raw material in the form of sawmill chips can be processed into a specific final product, e.g. pellets. The process involves chip thickening under the action of external and internal forces applied to obtain a fixed shape and size of the pellet. Before the granulation, the chips must have adequate humidity, calorific value, colour, purity (free from such contaminants as bark, large pieces of wood, stones, or pieces of metal), as well as low ash content.

Drum and belt dryers are often used for drying sawdust. Each dryer for structural reasons has its limitations and disadvantages, e.g. their efficiency or use of exhaust gases for drying materials (WITROWA-RAICHTER 2009, STRUMILŁO 1983). Drying with exhaust gases causes colour changes in the sawdust and its demineralization and a higher ash content, which adversely affects the pelleting process (BERGSTRÖM 2008). This problem can be solved by drying sawdust with a hot air stream.

Fountain dryers with a vertical drying chamber allow the material to be dried in a very efficient way and dispersing the material by creating a fountain effect. The scattered, detached material can also be dried with hot air instead of exhaust gases. However, fountain dryers are mainly used for drying granular materials of equal size and weight, e.g. cereal grains. Hence, during drying sawdust in a typical fountain dryer, there are several process difficulties, particularly the formation of a slugging effect, limiting the amount of dried material.

The main aim of this work is an analysis of the possibility of using a fountain dryer to dry pine sawdust for pellet production. This paper presents the results of research work on selected physicochemical properties of pine shavings obtained from various sawmills in the Knyszyńska Forest and proposes an improved fountain dryer for drying wet sawdust.

Material and methods

Two measurements presented in this article relate to the fountain drying process, i.e. the stand for testing the flow of loose materials and the sawdust drying process characterization (drying curves). The rest of the measurements and tests refer to the sawdust material. The tested sawdust was collected from various pine trees, i.e. from wood that was fresh, rotten and exposed for a long time for different weather conditions. Trees were also cut at different seasons.

In the case of pellet production, a large amount of sawdust is needed. Therefore, the authors in this work wanted to represent the real conditions encountered in granulate production.

Sawdust material

Sawdust resulting from the machining of wood has a shape and size mainly dependent on the cutting tools, process parameters and the physicochemical properties of wood.

In general, chip morphology is mainly dependent on the type of machining tool used, an example of which is presented in Figure 1. Due to its high availability, pine sawdust obtained from a band sawmill was chosen for this study (Fig. 1*a*). Figs. 1*b* and 1*c* show chip morphology obtained using a frame sawmill and a wood milling machine, respectively.

Due to an increased tooth size in the frame sawmill and the reciprocating movement of the tool, these chips are much larger compared to the chips obtained from a band sawmill. Such sawdust has the shape of sticks of varying lengths. The shape of the chips obtained on the wood milling machine is defined by the geometry of the milling cutter and they are thick and twisted.



Fig. 1. Examples of the morphology of pine sawdust obtained from various cutting devices: *a* – sawdust from a band sawmill, *b* – sawdust from a frame sawmill, *c* – sawdust from a milling machine

Sawdust testing methods

A representative sample of pine sawdust from a band sawmill (Fig. 1a) with a mass of 10 kg and an average moisture content of $46 \pm 2\%$ was collected and secured. The chips were sealed in hermetic containers and then used for further testing of their properties. To determine the morphology and selected physicochemical properties of the pine sawdust, the following tests and observations were carried out:

- calorific value, using a caloric bomb (Parr 6100);
- ash content, by burning samples in the oven (Nabertherm P330);
- microscopic observations, using an SEM equipped with an EDS device (Hitachi 3000N) and an optical microscope (Olympus 2000);
- chip-specific surface area, using the BET method;
- sawdust drying process (for establishing drying curves as a function of temperature), using a dryer (Radwag MA 50R);
- size distribution of wet sawdust and after drying, using the ImageJ program;
- sawdust sieving analysis.

In addition, sawdust was fed to various thermal treatments, in a thermal furnace and in a drum dryer at 400°C , where the drying agent was exhaust gas.

A selected sample of 0.4 kg was used to determine the calorific value of pine sawdust. The sawdust sample was placed on trays and dried until the mass stabilized. The mass of the sample was measured every 1 h. Then, after stabilization, moisture was measured using a moisture analyser and was $8.2 \pm 0.1\%$. Further, 15 representative 0.01 kg specimens were selected again and were ground in a small kit mill and pressed into a pellet with a diameter of 20 mm and a height of about 14 mm. The specimens were precisely weighed and then tested with a calorimetric bomb (Parr 6100). The operating parameters of the calorimetric bomb are given: oxygen for combustion – $\text{O}_2 = 99.95\%$; working pressure – $P = 30$ bar; weight of separated water – $m_w = 2$ kg.

For the ash content testing, 30 samples of dried sawdust, with 0.5% of humidity and 0.001 kg mass were used for a single sample. Sawdust samples were placed in pre-weighed crucibles. The crucibles were placed in a laboratory oven (Nabertherm P330) and allowed to burn. After cooling, the samples were weighed with a laboratory balance with an accuracy of 0.001×10^{-3} kg. The ash content was determined indirectly using formula (1).

$$A = \frac{m_3 - m_1}{m_2 - m_1} \cdot 100\% \quad [\%_{\max}] \quad (1)$$

where:

- A – is the content of volatiles in the analytical sample $[\%_{\max}]$,
- m_1 – is the mass of the crucible,

m_2 – is the mass of the crucible with the raw material being burnt,
 m_3 – the mass of crucible with ashes.

A scanning electron microscope (SEM) and optical microscope (OM) were used to study the microstructure of both wet and dry sawdust samples. Samples of varying humidity (from 5% to 46%) were observed. Due to the scattering of light in the water contained in the samples during OM observations, to increase the contrast of the chips, they were dyed blue with ink.

Examinations of the specific surface area of the sawdust were also performed using the BET method. The sawdust samples were inserted into a chamber with nitrogen penetrating the surface of the material. By knowing the pressure, temperature and gas volume, one can calculate how much gas has been absorbed on the chip surface based on the mass difference. Using formula (2), the specific surface area of the wet and dry sawdust was calculated.

$$S_p = a_p \cdot N \cdot w_p \quad (2)$$

where:

N – the Avogadro's number,

w_p – the surface occupied by a particle in the surface of the test sample,

a_p – the amount of the gas absorbed.

Three humid (46% of moisture) samples of 0.01 kg each were used for the sawdust drying tests, to dry them by $5 \pm 2\%$. For the analysis of phenomena occurring during the drying process of sawdust, so-called drying curves were used, as a function of drying time and temperature. A moisture analyser (AGS200) was applied for the tests. The tests were carried out for three temperatures 100°C, 125°C and 150°C, repeating each of them three times.

Measuring the size of sawdust, using computer image analysis method, the change in the equivalent diameter of chips before and after drying was determined. An example image of the sawdust before drying and after drying is presented in Figure 2. A series of sawdust images were taken. The best quality photos were then selected, scaled, converted and automatically analysed by the computer program (ImageJ). 500 wet chips and 500 dry chips were analysed.

Observations of sawdust motion kinematics in the fountain stand (Fig. 3) were performed. This study was intended to visualize and analyse the processes occurring in the fountain bed. The fountain test stand (Fig. 3) consists of a glass pipe 1 through which air was pumped at a given speed by a fan 6, controlled using an inverter and a throttle valve 5. The amount of airflow was measured by rotameter 3, so it was possible to precisely set the flow. The single test duration was 10 minutes. The entire fountain process was recorded with camera 4.

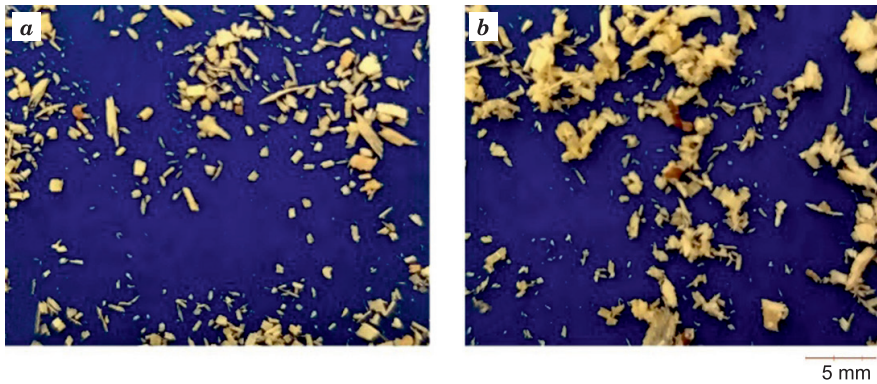
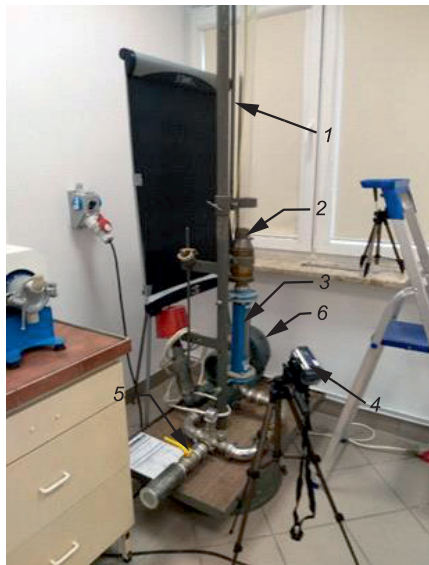


Fig. 2. Image of samples of sawdust: *a* – dry sawdust of 5% humidity, *b* – wet sawdust of 46% humidity



1 – glass pipe with an internal diameter of 50 mm, 2 – perforated baffle, 3 – rotameter, 4 – camera, 5 – throttle valve, 6 – fan

Fig. 3. Research stand for testing the flow of loose materials at the Faculty of Civil Engineering, in BUT

Samples with three different humidity levels (46%, 37%, 28%) were prepared for the testing. In the first phase, a flow rate of $600 \text{ dm}^3/\text{h}$ was established for sawdust volume of 100 ml. The parameters of the stand are presented below: testing time – $t_1 = 10 \text{ min}$; flow rate – $S = 600 \text{ dm}^3/\text{h}$; sample volume – $V = 100 \text{ ml}$; air temperature – $t_2 = 22,5^\circ\text{C}$; air humidity – $Y_p = 50\%$. Sawdust moisture before drying: $Y_1 = 46\%$, $Y_2 = 37\%$, $Y_3 = 28\%$. Sawdust moisture after drying: $Y_1' = 22\%$, $Y_2' = 7\%$, $Y_3' = 5\%$.

The sieving analysis of chips with different humidity was also carried out using the Multiserw LPzE-2e laboratory shaker. Sieves were set up in accordance with PN-EN-ISO 3310. Three 0.01 kg samples obtained after drying in the fountain bed were used.

Results and discussion

Calorific value

The calorific value for the dried pine chips was 18.07 MJ/kg, which is similar to the data described in the literature (NINGBO 2015). Using a low vacuum SEM-EDS analysis, the chemical composition of the pine chips was detected. The pine sawdust consists of: C – 53.9%, O – 40.1%, K – 0.01%, S – 0.005%, Cl – 0.005%. Similar chemical composition was reported in the literature (KAJDA-SZCZEŚNIAK 2013). A slightly different composition was obtained from other regions of Europe (DOS SANTOS VIANA 2018).

Ash content

The average ash content after drying the sample in the stand presented in Figure 3 was 0.504 ± 0.15 . This is a similar amount of ash obtained by other authors (GLIJER 2011, JIRJIS 1995, BRYŚ 2016). Ash content was also tested for dried sawdust in a conventional drum dryer, where the drying medium is exhaust gases. The ash content was 0.743 ± 0.12 (Fig. 4).

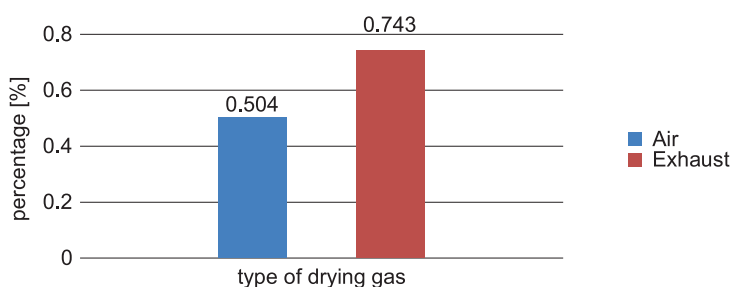


Fig. 4. Ash content depending on the method of drying with dried air and exhaust fumes

It can be noted that the ash content in sample dried in exhaust gases is 25% higher compared to sawdust dried in a fountain bed. This is because the exhaust gases contain ash particles that settle on the surface of the wood chip. Note that the pine samples used for these comparative tests were taken

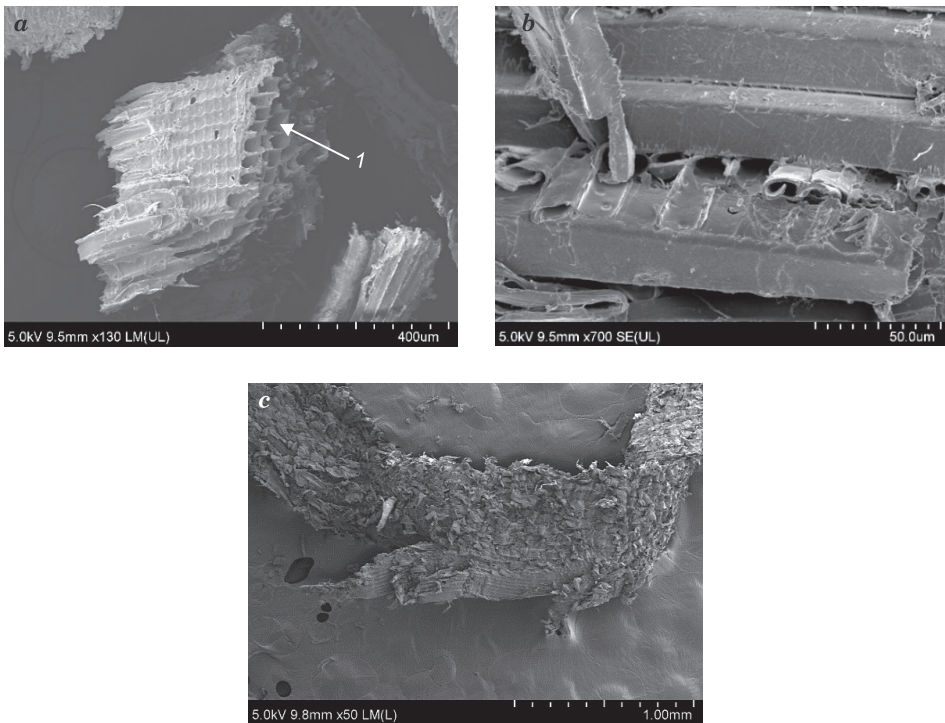
from an industrial drum dryer, which was equipped with firewalls with settling chambers for particle separation from the exhaust gases.

The percentage of ash content essentially affects the quality of the raw material. During the production of fuel pellets, the amount of hard ash particles should be as low as possible. Too much of them can lead to clogging the furnace burners in which solid fuel in the form of granules is burned.

Additionally, ash settling on the chip surface causes a colour change to darker pellets, which is not desired by customers and results in a lower price of the product. Therefore, hot air drying as opposed to exhaust gases is proposed.

Microscopic observations

To determine the water retention in the chips and the processes that occur during their drying, several microscopic observations of the samples were carried out. Literature reports (STRUMILLO 2006, KUDRA, MUJUMDAR 2009, PERRE, KEY



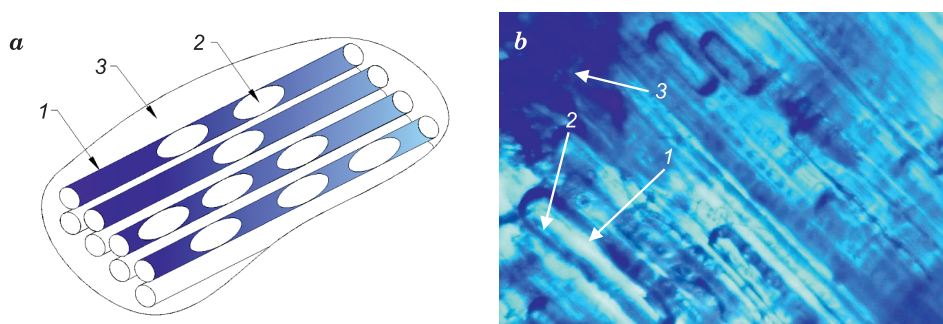
I – capillary

Fig. 5. Chip structure (a, dry sawdust), channel permeability in a chip (dry) (b), SEM image of a surface of a single pine chip (dry sawdust) (c)

2006) show that the water in the wet material is located inside the growth cells, on the surface and between the wood chips.

Microscopic observations show that the water contained inside the wood cells (capillary 1, Fig. 5a) can lead to changes in chip morphology as a result of intensive drying. This phenomenon is observed during rapid heating of small pieces of sawdust.

Capillaries in a tree form channels where water and nutrients are transported. Depending on the degree of humidity, these channels may be partially filled with water or air (Figs. 6a and 6b). During the drying process, a rapid increase in gas pressure in the ducts can cause cracking (tearing) of chips, which leads to an increase in the amount of a small fraction. This process is desirable for pellet production because more small fractions result in better granule quality (BERGSTRÖM 2008).



1 – capillary, 2 – air bubble, 3 – cell walls of the wet chip
 Fig. 6. Schematic view of the water in the wet chip (a), OM image of a wet chip filled with water and air bubbles (b) (magnification $\times 50$, description in the text)

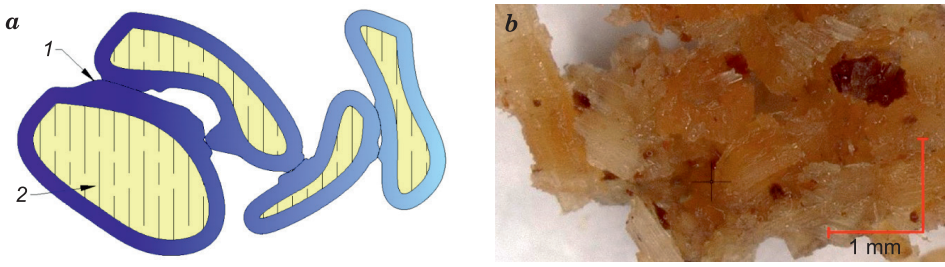
In Figure 6b, the light areas (1) show air bubbles inside the cells, while the dark areas are coloured water (3). The number (2) indicates the interface between water and air. Microstructure observations confirmed that the water inside the wood chip did not completely fill the internal cells.

The temperature gradient on the chip, as a result of drying, can cause internal stress due to different thermal expansion of the chip. This causes chip twisting (warping) and wood shrinkage, which results in its structure changing during drying. This shrinkage is the greatest along the capillaries. Thus, the shrinkage will be different depending on the location of the tree trunk which the chip comes and the way how it is obtained.

Moreover, the chips resulting from cutting have channels with various levels of permeability (Fig. 5b) which makes it difficult to remove the water remaining from inside the crushed tubes. This also leads to the process of chips cracking described above. Water on the chip surface is also a significant reservoir that

must be evaporated in the process of drying. Due to the highly developed specific surface area, numerous capillary's and cavities, the chips accumulate water drops on the top layers. In the case of lower humidity, water does not fill the entire surface tightly but stays in the form of drops embedded in the insets. Water also occurs in a general mass of sawdust between individual particles of chips (Figs. 7a and 7b), which can be much more humid than the rest of the material. This water can get into the sawdust during rainfall or high humidity. Sawdust at high humidity sticks together, forming large agglomerations.

While the process of evaporation of this water from the chip surface is fast (GLIJER 2011), exposure of sawdust in high humidity conditions for too long causes water to enter. This is because the size of a single H₂O molecule is 0.28 nm (PANG 2014) and therefore it may easily penetrate the chips.



1 – water bridges, 2 – chip (wet sawdust)

Fig. 7. Drawing showing water accumulation between chips (a), water between the chips forms agglomerates (wet sawdust) (b)

Specific surface area

The specific surface area of sawdust measured for the dry sample, with $5 \pm 2\%$ of humidity, and for the wet sample, with $46 \pm 2\%$ humidity, is $0.5233 \text{ m}^2/\text{g}$ and $0.5826 \text{ m}^2/\text{g}$, respectively.

In analysing these results, one can conclude that the dry sample has an approx. 10% smaller specific surface area compared to the wet sample. This is caused by the shrinking of wood, due to the evaporation of water, which during the drying process leaves the cells and thereby reduces their size. The wood shrinkage depends on the fibre direction, e.g. wood shrinks 1.7 times less in the radial direction and this is 20 times less in the longitudinal direction than in the tangential direction. It should be mentioned that this phenomenon occurs for sawdust of 30% and lower humidity, as it is reported in (GLIJER 2011, PERRE, KEYEY 2006).

Determination of chip drying characteristics

The drying process of chips with a humidity of 46% as a function of time and temperature is presented in Figure 8. In the drying process, three characteristic stages can be distinguished.

Stage 1 is the period in which the heated chips have negligible weight loss. This stage includes the ranges: T_1 , T_2 , T_3 , and for three temperatures, which are equal in time, lasts about 60 seconds and does not depend on the temperature.

Stage 2 with ranges of T_{21} , T_{22} , T_{23} are of different length (time axis) and depend on the drying temperature. The T_{21} section at 150°C is the shortest and lasts about 590 s. Compared with the drying time at 100°C, the drying time increases to 1,000 s and it is 59% longer.

Stage 3 shows a plateau, where no changes in chip mass were observed. This means that the process of water evaporation has been completed and only the dry mass of sawdust remained (STRUMILLO 2006).

The drying curves show the starting parameters for the further comparative analysis of the drying process of the pine sawdust. They were made in heating conditions without airflow. Thanks to this, by comparing them with the drying curves on the test stand, we can see how other parameters, such as blowing speed, temperature or the type of bed affect the drying speed.

The obtained results may suggest that in certain weather conditions it is reasonable to pre-heat the sawdust before drying. Thus, in the autumn-winter period, when the sawdust is very moist, the drying time can be significantly reduced. Pre-heating of the sawdust can be carried out outside the drying

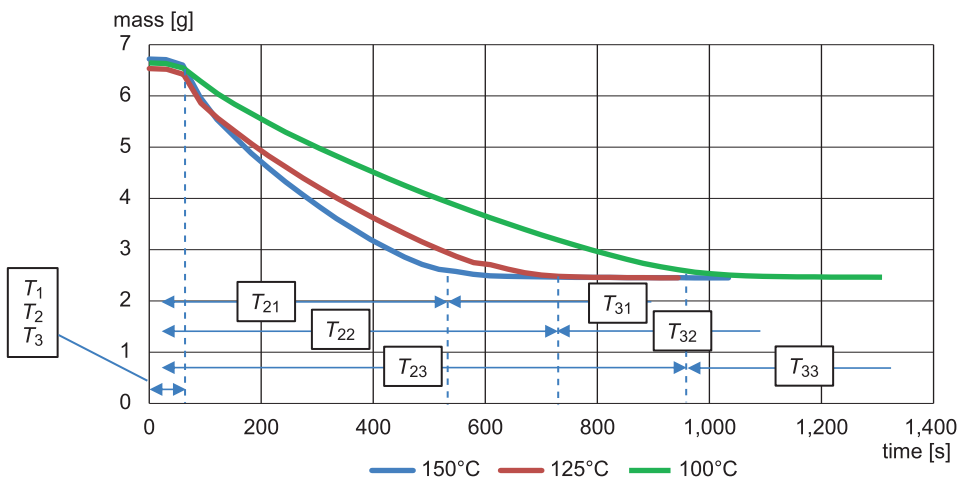


Fig. 8. Drying curves of the wet pine sawdust tested at 100°C, 125°C and 150°C, respectively, made with a moisture analyser

chamber, e.g. in screw feeders. The advantage of pre-heating has been confirmed by literature (WITROWA-RAICHTER 2009, KEEY 1991, DE LA FUENTE-BLANCO, DE SARABIA 2006, BRYŚ 2016).

Image analysis of sawdust before and after drying

This section presents the histogram (Fig. 9) of the dry and wet chip fraction distributions presented from images in Figure 2. From the graph, one can conclude that the highest percentage of the chip size is 0.5 mm, both wet and dry and that the total proportion of particles smaller than 0.5 mm is greater for dry chips with 5% of moisture. This confirms that crushing and cracking of the sawdust occurs during the drying process.

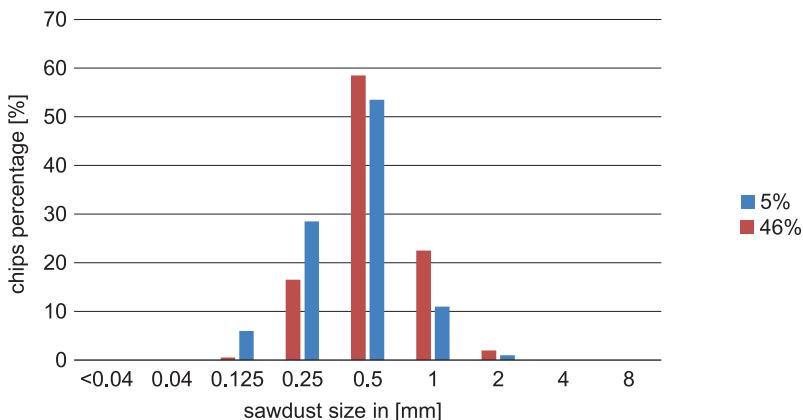


Fig. 9. Image analysis of the chip size distribution with different humidity: 5% and 46%, respectively

Analysing the results presented in Figure 9, it can be concluded that the average wet chip size is approximately 22% larger than the dry chip size. The average chip sizes are similar to those reported in the literature (GLIJER 2011, PERRE, KEEY 2006). Furthermore, after drying, the chips are in the range from 0.125 to 2.0 mm. Note that the large chips are undesirable, interfering with the drying process in a fountain dryer. However, they constitute only about 1% of the entire percentage of the vortices. However, the smallest chips constitute about 5% of the total value, and they are desirable during the granulation process. Although they may have a few percent higher humidity compared to larger chips, the water evaporates faster due to their lower weight.

Sieving analysis

Figure 10 presents images of the pine sawdust after sieving analysis of drying in the fountain bed, whereas Figure 11 presents a histogram of chip size distribution with different humidity (45%, 37% and 28%, respectively). Based on the obtained results, the data of the sieve analysis generally coincide with the results of the image analysis, in which about 90% of the chips are in the range of 0.125-1.0 mm, and chip moisture affects particle size distribution.

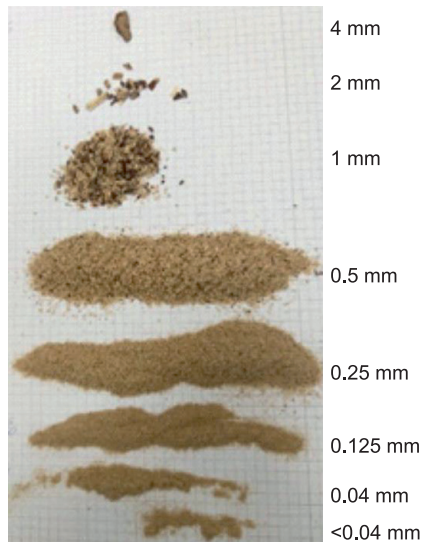


Fig. 10. Sawdust fractions obtained by sieving analysis of sawdust with an initial moisture content of 37%

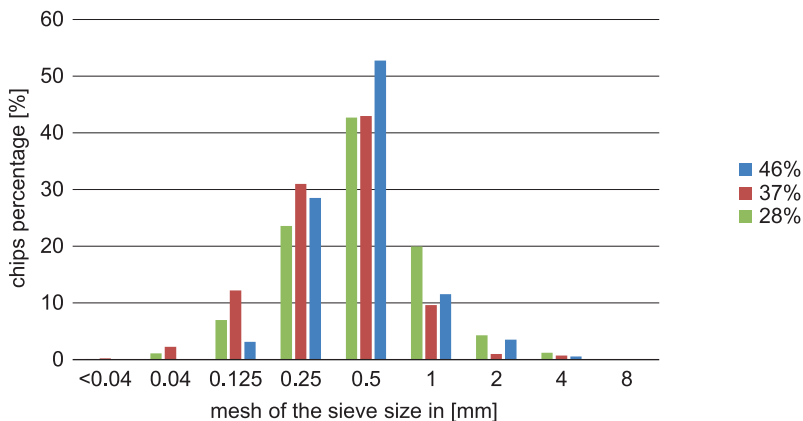


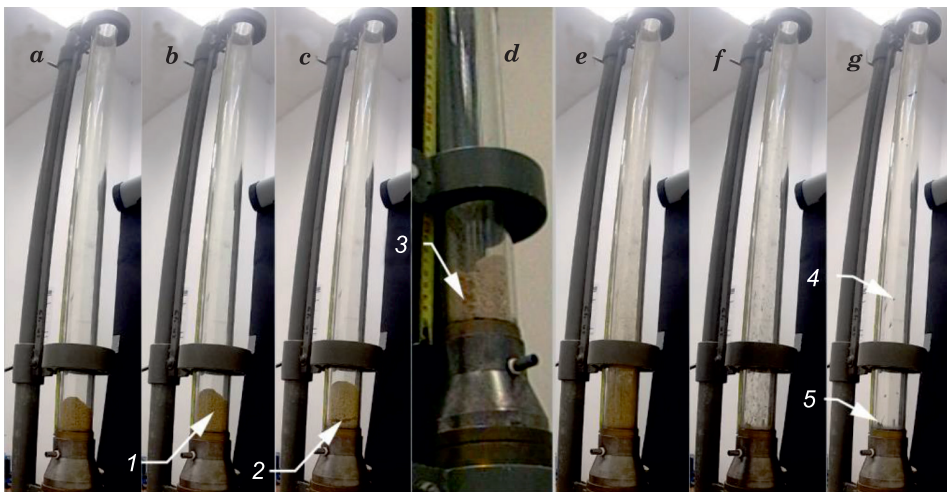
Fig. 11. Percentage distribution of wet chips after drying on the test stand

Figure 11 shows that there are ~ 45% of 0.5 mm chips, ~ 28% of chips are 0.25 mm in size, and ~ 8% of sawdust is 0.125 mm. There is also about 3% of the undesirable, coarse shavings fraction with an average particle size of 1, 2 and 4 mm (Fig. 10) which have bark and other impurities. The high content of the bark has a negative influence on the granulation process, e.g. increasing the ash content and changing the colour. Thus, a good solution is to use the bark for incineration in a furnace feeding a dryer.

Further technical solutions for the fountain dryer will be proposed to eliminate the coarse particles from the sawdust.

Motion kinematics research in the fountain bed

Figure 12 shows the stages of the formation of a fountain bed during the drying of the chips on the stand presented in Figure 3. Chips with a moisture content of 46%, 37%, and 28% were used. The moisture of the chips after the drying process ranged from 5-8%. When analysing the movement of particles (sawdust) in the fountain bed, several basic stages can be distinguished. Turning on the fan resulted in the bulging of the bed surface (the so-called “loosening”) combined with an increase in volume (Fig. 12*b*). There is also the phenomenon



1 – volume increase, 2 – crack of the bed, 3 – channel interrupting the bed, 4 – levitating chips, 5 – chips not involved in the process of fountaining

Fig. 12. Stages occurring in the fountain bed during drying of the sawdust for 10 minutes: *a* – initial state, *b* – loosening, *c* – delamination, *d* – the interruption of stream continuity, *e* – the formation of a proper spouted bed, *f* – gradual reduction in the number of chips, *g* – residues after drying

of a further increase in the volume of the bed (Fig. 12c). The interruption of stream continuity and the formation of a trough inside the bed is the next stage of the process shown in Figure 12d. The formation of a proper spouted bed and a gradual reduction in the number of chips inside the pipe are shown in Figure 12e and 12f. Note, that “levitating chips” (4) in Figure 12g were also observed which were not able to leave the drying chamber even after a long drying period. These individual chips are not involved in the fountain process and eventually fell to the bottom of the pipe. From these observations, it appears that one can distinguish the stages: a fixed, bubbling bed (Fig. 12a, 12b and 12c) and a rapid transition to a turbulent bed, followed by rapid fluidization (Fig. 12e) (GUPTA, SATHIYAMOORTHY 1999).

Based on the obtained results, it can be concluded that the time needed to dry the chips in the fountain bed is much shorter than when drying the chips with a moisture analyser. During 600 seconds of fountain drying, a 0.1 kg sample of sawdust was dried to a moisture content of 5-8%, blowing the material with 25°C air. This is because there can a large volume of airflow in a short time in the fountain bed with very intensive turbulent chip mixing.

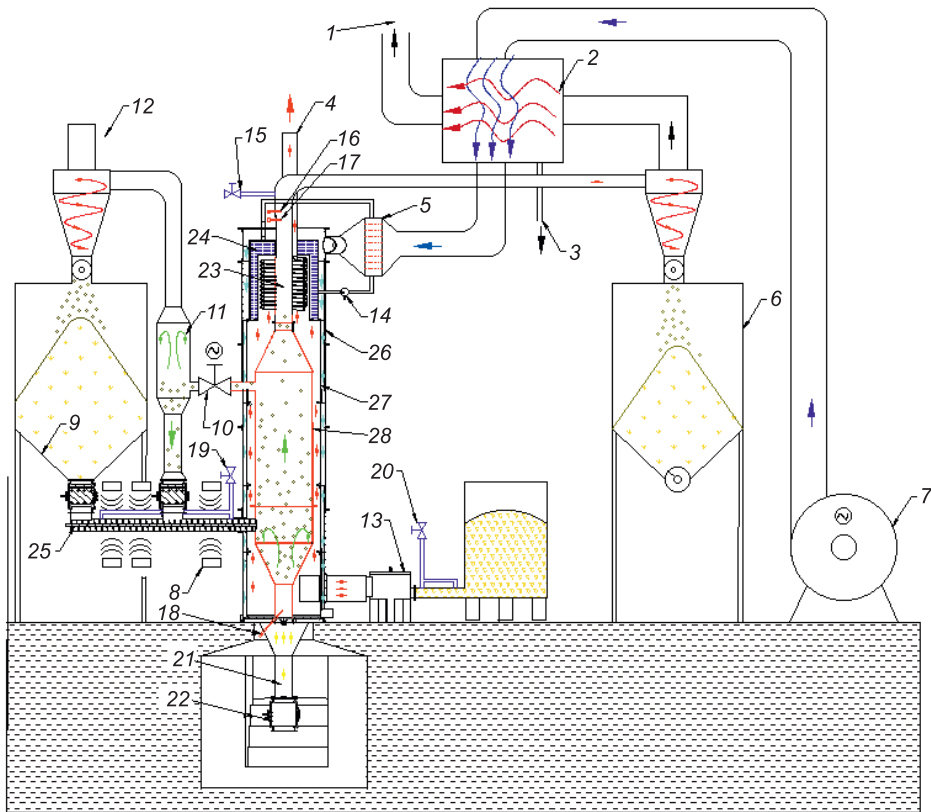
Improvements proposed in a foundation dryer

In analysing the process of drying chips in the fountain bed, the most significant problem discovered is sawdust pollution and large-size chips. To solve these problems, based on literature analysis (MUJUMDAR 2006, KUDRA 2004, LIU 2014, AZIZ 2011, ZHANG 2017) and on the results of preliminary research work, the authors proposed several modifications and improvements in the construction of a fountain dryer. Figure 13 shows a design solution for a fountain dryer to improve the drying process of heterogeneous materials, in this case, of pine sawdust. Note that such devices are usually used for drying homogeneous materials, e.g. powders, corns, etc.

The proposed device (Fig. 13) has the following modifications compared with a typical fountain dryer:

- bed adjustment valve 10;
- cone separator for removing stones, metal pieces, bark 22;
- an internal system of heating air by flue exhaust gas 27;
- water heater 24;
- ultrasound heating generators 8.

The introduced improvements are designed to obtain a dried product with appropriate technological properties, i.e. sawdust with parameters necessary for the production of fuel pellets. The next step is to improve the thermal and functional properties of the dryer.



1 – air outlet, 2 – recuperator, 3 – condensate outlet – dehydration, 4 – exhaust outlet, 5 – water heater, 6 – dry sawdust tank, 7 – fan, 8 – ultrasonic generator, 9 – raw material tank, 10 – air cushion adjustment valve, 11 – sawdust separator, 12 – cyclone, 13 – furnace, 14 – water pump, 15 – water inlet to extinguish (extinguishing system), 16 – flowmeter, 17 – thermocouple (temperature measurement at the output), 18 – thermocouple (input temperature measurement), 19 – water inlet for cooling the material in the screw feeder, 20 – water inlet to extinguish the raw material in the screw feeder, 21 – heavy debris discharge, 22 – rotary sluice, 23 – air outlet from the drying chamber, 24 – water heater with flue gas, 25 – screw conveyor, 26 – external case, 27 – inside case, 28 – drying chamber

Fig. 13. Scheme of the proposed fountain dryer

Summary

This work aimed to propose a new design of a fountain dryer, to provide an optimal product for the production of pine pellets.

This article presents an analysis of pine sawdust obtained from the Knyszyńska forest and its drying process, which is the first stage of the pellet production. The drying process in fountain dryers of heterogeneous sawdust

materials is difficult due to non-homogeneous material. Different particle sizes hinder the proper functioning of the bed. They also have impurities which also affect the operation of the bed and cause the dry material to have worse technological properties in terms of further granulation. Therefore, the fountain dryer should be equipped with tools and devices that can separate the least valuable big sawdust particles, metal parts, bark, stones and other impurities. Thus, the basic parameters of the sawdust were determined, i.e. the chemical composition, calorific value, surface area analysis, sieve analysis and ash content for drying process performed by exhausted gases and hot air. Analysis of the ash content showed a significant reduction of the ash for the samples dried by warm air in comparison to the exhaust gases (drum dryer). The BET analysis revealed that after drying, the surface area of the sawdust decreased by approximately 10%. A series of microscopic observations were also carried out to analyse the manner of water accumulation in sawdust and the effect of water evaporation on the sawdust morphology. In analysing the kinematics of the sawdust sample movement in the fountain bed, it can be concluded that the bed movement during the fountain process is affected by the size and morphology of the particles.

Based on the literature, research work and the authors' own experience, a modification of a typical fountain dryer was proposed. Thanks to this modification, the fountain dryer will be able to dry the sawdust with exhaust gases without contaminating them with additional sorting of coarse fractions that often interrupt the fountain process.

References

- AZIZ M., FUSHIMI C., KANSHA Y. 2011. *Innovative Energy-Efficient Biomass Drying Based on Self-Heat Recuperation Technology*. Wiley Online Library.
- BERGSTRÖM D., ISRAELSSON S., ÖHMAN M., DAHLQVIST S.A., GREF R., BOMAN C., WÄSTERLUND I. 2008. *Effects of raw material particle size distribution on the characteristics of Scots pine sawdust fuel pellets*. Fuel Processing Technology, 89(12): 1324-1329.
- BRYŚ A., BRYŚ J., OSTROWSKA-LIGEŻA E., KALETA A., GÓRNICKI K., GŁOWACKI S., KOCZOŃ P. 2016. *Wood biomass characterization by DSC or FT-IR spectroscopy*. Journal of Thermal Analysis and Calorimetry, 126(1): 27-35.
- FUENTE-BLANCO S. DE LA, SARABIA E.R.F. DE, ACOSTA-APARICIO V.M., BLANCO-BLANCO A., GALLEGUO-JUÁREZ J.A. 2006. *Food drying process by power ultrasound*. Ultrasonics, 44: e523-e527.
- GLLJER L. 2011. *Suszenie drewna*. Wydawnictwo „Wież Jutra”, Warszawa.
- GUPTA C.K., SATHIYAMOORTHY D. 1998. *Fluid bed technology in materials processing*. CRC press, Boca Raton, Florida.
- Handbook of drying of vegetables and vegetable products*. 2017. Eds. M. Zhang, B. Bhandari, Z. Fang. CRC Press, Boca Raton, Florida.
- JIRJIS R. 1995. *Storage and drying of wood fuel*. Biomass and Bioenergy, 9(1-5): 181-190.
- KAJDA-SZCZEŚNIAK M. 2013. *Evaluation of the basic properties of the wood waste and wood based wastes*. Archives of Waste Management and Environmental Protection, 15(1): 1-10.
- KEY R.B. 1991. *Drying of loose and particulate materials*. CRC Press, Boca Raton, Florida.
- KUDRA T. 2004. *Energy aspects in drying*. Drying Technology, 22(5): 917-932.

- KUDRA T., MUJUMDAR A.S. 2009. *Zaawansowane technologie suszenia*. CRC Press, Boca Raton, Florida.
- LIU Y., PENG J., KANSHA Y., ISHIZUKA M., TSUTSUMI A., JIA D., SOKHANSANJ S. 2014. *Novel fluidized bed dryer for biomass drying*. Fuel Processing Technology, 122: 170-175.
- MUJUMDAR A.S. 2006. *Principles, classification, and selection of dryers*. In: *Handbook of industrial drying*. CRC Press, Boca Raton, Florida.
- MUJUMDAR A.S., LAW C.L. 2010. *Drying technology: Trends and applications in postharvest processing*. Food and Bioprocess Technology, 3(6): 843-852.
- NINGBO G., BAOLING L., AIMIN L., JUANJUAN L. 2015. *Continuous pyrolysis of pine sawdust at different pyrolysis temperatures and solid residence times*. Journal of Analytical and Applied Pyrolysis, 114: 155-162.
- NOSEK R., HOLUBCIK M., JANDACKA J. 2016. *The impact of bark content of wood biomass on biofuel properties*. BioResources, 11(1): 44-53.
- PANG X.F. 2014. *Water: molecular structure and properties*. World Scientific, Singapur.
- PERRE P., KEEY, R.B. 2006. *Drying of wood: principles and practices*. In: *Handbook of industrial drying*. CRC Press, Boca Raton, Florida.
- SANTOS VIANA, H.F. DOS, MARTINS RODRIGUES A., GODINA R., OLIVEIRA MATIAS, J.C. DE, RIBEIRO NUNES L.J. 2018. *Evaluation of the physical, chemical and thermal properties of Portuguese maritime pine biomass*. Sustainability, 10(8): 2877.
- SCHERER V., MÖNNIGMANN M., BERNER M.O., SUSBROCK F. 2016. *Coupled DEM-CFD simulation of drying wood chips in a rotary drum – Baffle design and model reduction*. Fuel, 184: 896-904.
- STRUMILLO C. 1986. *Suszenie: zasady, zastosowania i projekt*. Tom 3. CRC Press, Boca Raton, Florida.
- STRUMILLO C. 2006. *Perspectives on developments in drying*. Drying Technology, 24(9): 1059-1068.
- WITROWA-RAICHTER D. 2009. *New trends in food drying*. AgEngPol, Warszawa.

Guide for Authors

Introduction

Technical Sciences is a peer-reviewed research Journal published in English by the Publishing House of the University of Warmia and Mazury in Olsztyn (Poland). Journal is published continually since 1998. Until 2010 Journal was published as a yearbook, in 2011 and 2012 it was published semiyearly. From 2013, the Journal is published quarterly in the spring, summer, fall, and winter.

The Journal covers basic and applied researches in the field of engineering and the physical sciences that represent advances in understanding or modeling of the performance of technical and/or biological systems. The Journal covers most branches of engineering science including biosystems engineering, civil engineering, environmental engineering, food engineering, geodesy and cartography, information technology, mechanical engineering, materials science, production engineering etc.

Papers may report the results of experiments, theoretical analyses, design of machines and mechanization systems, processes or processing methods, new materials, new measurements methods or new ideas in information technology.

The submitted manuscripts should have clear science content in methodology, results and discussion. Appropriate scientific and statistically sound experimental designs must be included in methodology and statistics must be employed in analyzing data to discuss the impact of test variables. Moreover there should be clear evidence provided on how the given results advance the area of engineering science. Mere confirmation of existing published data is not acceptable. Manuscripts should present results of completed works.

There are three types of papers: a) research papers (full length articles); b) short communications; c) review papers.

The Journal is published in the printed and electronic version. The electronic version is published on the website ahead of printed version of Technical Sciences.

Technical Sciences does not charge submission or page fees.

Types of paper

The following articles are accepted for publication:

Reviews

Reviews should present a focused aspect on a topic of current interest in the area of biosystems engineering, civil engineering, environmental engineering, food engineering, geodesy and cartography, information technology, mechanical engineering, materials science, production engineering etc. They should include all major findings and bring together reports from a number of sources. These critical reviews should draw out comparisons and conflicts between work, and provide an overview of the 'state of the art'. They should give objective assessments of the topic by citing relevant published work, and not merely present the opinions of individual authors or summarize only work carried out by the authors or by those with whom the authors agree. Undue speculations should also be avoided. Reviews generally should not exceed 6,000 words.

Research Papers

Research Papers are reports of complete, scientifically sound, original research which contributes new knowledge to its field. Papers should not exceed 5,000 words, including figures and tables.

Short Communications

Short Communications are research papers constituting a concise description of a limited investigation. They should be completely documented, both by reference list, and description of the experimental procedures. Short Communications should not occupy more than 2,000 words, including figures and tables.

Letters to the Editor

Letters to the Editor should concern with issues raised by articles recently published in scientific journals or by recent developments in the engineering area.

Contact details for submission

The paper should be sent to the Editorial Office, as a Microsoft Word file, by e-mail: techsci@uwm.edu.pl

Referees

Author/authors should suggest, the names, addresses and e-mail addresses of at least three potential referees. The editor retains the sole right to decide whether or not the suggested reviewers are used.

Submission declaration

After final acceptance of the manuscript, the corresponding author should send to the Editorial Office the author's declaration. Submission of an article implies that the work has not been published previously (except in the form of an abstract or as part of a published lecture or academic thesis or as an electronic preprint), that it is not under consideration for publication elsewhere, that publication is approved by all authors and tacitly or explicitly by the responsible authorities where the work was carried out, and that, if accepted, it will not be published elsewhere in the same form, in English or in any other language.

To prevent cases of ghostwriting and guest authorship, the author/authors of manuscripts is/are obliged to: (i) disclose the input of each author to the text (specifying their affiliations and contributions, i.e. who is the author of the concept, assumptions, methods, protocol, etc. used during the preparation of the text); (ii) disclose information about the funding sources for the article, the contribution of research institutions, associations and other entities.

Language

Authors should prepare the full manuscript i.e. title, abstract and the main text in English (American or British usage is accepted). Polish version of the manuscript is not required.

The file type

Text should be prepared in a word processor and saved in doc or docx file (MS Office).

Article structure

Suggested structure of the manuscript is as follows:

Title

Authors and affiliations

Corresponding author

Abstract

Keywords

Introduction

Material and Methods

Results and Discussion

Conclusions

Acknowledgements (optional)
References
Tables
Figures

Subdivision – numbered sections

Text should be organized into clearly defined and numbered sections and subsections (optionally). Sections and subsections should be numbered as 1. 2. 3. then 1.1 1.2 1.3 (then 1.1.1, 1.1.2, ...). The abstract should not be included in numbering section. A brief heading may be given to any subsection. Each heading should appear on its own separate line. A single line should separate paragraphs. Indentation should be used in each paragraph.

Font guidelines are as follows:

- Title: 14 pt. Times New Roman, bold, centered, with caps
- Author names and affiliations: 12 pt. Times New Roman, bold, centered, italic, two blank line above
- Abstract: 10 pt. Times New Roman, full justified, one and a half space. Abstract should begin with the word Abstract immediately following the title block with one blank line in between. The word Abstract: 10 pt. Times New Roman, centered, indentation should be used
- Section Headings: Not numbered, 12 pt. Times New Roman, bold, centered; one blank line above
- Section Sub-headings: Numbered, 12 pt. Times New Roman, bold, italic, centered; one blank line above
- Regular text: 12 pt. Times New Roman, one and a half space, full justified, indentation should be used in each paragraph

Title page information

The following information should be placed at the first page:

Title

Concise and informative. If possible, authors should not use abbreviations and formulae.

Authors and affiliations

Author/authors' names should be presented below the title. The authors' affiliation addresses (department or college; university or company; city, state and zip code, country) should be placed below the names. Authors with the same affiliation must be grouped together on the same line with affiliation information following in a single block. Authors should indicate all affiliations with a lower-case superscript letter immediately after the author's name and in front of the appropriate address.

Corresponding author

It should be clearly indicated who will handle correspondence at all stages of refereeing and publication, also post-publication process. The e-mail address should be provided (footer, first page). Contact details must be kept up to date by the corresponding author.

Abstract

The abstract should have up to 100-150 words in length. A concise abstract is required. The abstract should state briefly the aim of the research, the principal results and major conclusions. Abstract must be able to stand alone. Only abbreviations firmly established in the field may be eligible. Non-standard or uncommon abbreviations should be avoided, but if essential they must be defined at their first mention in the abstract itself.

Keywords

Immediately after the abstract, author/authors should provide a maximum of 6 keywords avoiding general, plural terms and multiple concepts (avoid, for example, 'and', 'of'). Author/authors should be sparing with abbreviations: only abbreviations firmly established in the field may be eligible.

Abbreviations

Author/authors should define abbreviations that are not standard in this field. Abbreviations must be defined at their first mention there. Author/authors should ensure consistency of abbreviations throughout the article.

Units

All units used in the paper should be consistent with the SI system of measurement. If other units are mentioned, author/authors should give their equivalent in SI.

Introduction

Literature sources should be appropriately selected and cited. A literature review should discuss published information in a particular subject area. Introduction should identify, describe and analyze related research that has already been done and summarize the state of art in the topic area. Author/authors should state clearly the objectives of the work and provide an adequate background.

Material and Methods

Author/authors should provide sufficient details to allow the work to be reproduced by other researchers. Methods already published should be indicated by a reference. A theory should extend, not repeat, the background to the article already dealt within the Introduction and lay the foundation for further work. Calculations should represent a practical development from a theoretical basis.

Results and Discussion

Results should be clear and concise. Discussion should explore the significance of the results of the work, not repeat them. A combined Results and Discussion section is often appropriate.

Conclusions

The main conclusions of the study may be presented in a Conclusions section, which may stand alone or form a subsection of a Results and Discussion section.

Acknowledgements

Author/authors should include acknowledgements in a separate section at the end of the manuscript before the references. Author/authors should not include them on the title page, as a footnote to the title or otherwise. Individuals who provided help during the research study should be listed in this section.

Artwork

General points

- Make sure you use uniform lettering and sizing of your original artwork
- Embed the used fonts if the application provides that option
- Aim to use the following fonts in your illustrations: Arial, Courier, Times New Roman, Symbol
- Number equations, tables and figures according to their sequence in the text
- Size the illustrations close to the desired dimensions of the printed version

Formats

If your electronic artwork is created in a Microsoft Office application (Word, PowerPoint, Excel) then please supply 'as is' in the native document format

Regardless of the application used other than Microsoft Office, when your electronic artwork is finalized, please 'Save as' or convert the images to one of the following formats (note the resolution requirements given below):

EPS (or PDF): Vector drawings, embed all used fonts

JPEG: Color or grayscale photographs (halftones), keep to a minimum of 300 dpi

JPEG: Bitmapped (pure black & white pixels) line drawings, keep to a minimum of 1000 dpi or combinations bitmapped line/half-tone (color or grayscale), keep to a minimum of 500 dpi

Please do not:

- Supply files that are optimized for screen use (e.g., GIF, BMP, PICT, WPG); these typically have a low number of pixels and limited set of colors
- Supply files that are too low in resolution
- Submit graphics that are disproportionately large for the content

Color artwork

Author/authors should make sure that artwork files are in an acceptable format (JPEG, EPS PDF, or MS Office files) and with the correct resolution. If, together with manuscript, author/authors submit color figures then Technical Sciences will ensure that these figures will appear in color on the web as well as in the printed version at no additional charge.

Tables, figures, and equations

Tables, figures, and equations/formulae should be identified and numbered consecutively in accordance with their appearance in the text.

Equations/mathematical and physical formulae should be presented in the main text, while tables and figures should be presented at the end of file (after References section). Mathematical and physical formulae should be presented in the MS Word formula editor.

All types of figures can be black/white or color. Author/authors should ensure that each figure is numbered and has a caption. A caption should be placed below the figure. Figure must be able to stand alone (explanation of all symbols and abbreviations used in figure is required). Units must be always included. It is noted that figure and table numbering should be independent.

Tables should be numbered consecutively in accordance with their appearance in the text. Table caption should be placed above the table. Footnotes to tables should be placed below the table body and indicated with superscript lowercase letters. Vertical rules should be avoided. Author/authors should ensure that the data presented in tables do not duplicate results described in figures, diagrams, schemes, etc. Table must be able to stand alone (explanation of all symbols and abbreviations used in table is required). Units must be always included. As above, figure and table numbering should be independent.

References

References: All publications cited in the text should be presented in a list of references following the text of the manuscript. The manuscript should be carefully checked to ensure that the spelling of authors' names and dates of publications are exactly the same in the text as in the reference list. Authors should ensure that each reference cited in the text is also present in the reference list (and vice versa).

Citations may be made directly (or parenthetically). All citations in the text should refer to:

1. Single author

The author's name (without initials, with caps, unless there is ambiguity) and the year of publication should appear in the text

2. Two authors

Both authors' names (without initials, with caps) and the year of publication should appear in the text

3. Three or more authors

First author's name followed by et al. and the year of publication should appear in the text

Groups of references should be listed first alphabetically, then chronologically.

Examples:

"... have been reported recently (ALLAN, 1996a, 1996b, 1999; ALLAN and JONES, 1995). KRAMER et al. (2000) have recently shown..."

The list of references should be arranged alphabetically by authors' names, then further sorted chronologically if necessary. More than once reference from the same author(s) in the same year must be identified by the letters "a", "b", "c" etc., placed after the year of publication.

References should be given in the following form:

KUMBHAR B.K., AGARVAL R.S., DAS K. 1981. Thermal properties of fresh and frozen fish. *International Journal of Refrigeration*, 4(3), 143–146.

MACHADO M.F., OLIVEIRA F.A.R., GEKAS V. 1997. Modelling water uptake and soluble solids losses by puffed breakfast cereal immersed in water or milk. In *Proceedings of the Seventh International Congress on Engineering and Food*, Brighton, UK.

NETER J., KUTNER M.H., NACHTSCHEIM C.J., WASSERMAN W. 1966. *Applied linear statistical models* (4th ed., pp. 1289–1293). Irwin, Chicago.

THOMSON F.M. 1984. Storage of particulate solids. In M. E. Fayed, L. Otten (Eds.), *Handbook of Powder Science and Technology* (pp. 365–463). Van Nostrand Reinhold, New York.

Citation of a reference as 'in press' implies that the item has been accepted for publication.

Note that the full names of Journals should appear in reference list.

Submission checklist

The following list will be useful during the final checking of an article prior to the submission. Before sending the manuscript to the Journal for review, author/authors should ensure that the following items are present:

- Text is prepared with a word processor and saved in DOC or DOCX file (MS Office).
- One author has been designated as the corresponding author with contact details: e-mail address
- Manuscript has been 'spell-checked' and 'grammar-checked'
- References are in the correct format for this Journal
- All references mentioned in the Reference list are cited in the text, and vice versa
- Author/authors does/do not supply files that are too low in resolution
- Author/authors does/do not submit graphics that are disproportionately large for the content